Constant-Thrust Orbital Transfer About Binary Asteroids Using Bilinear Tangent Guidance

ZICEN XIONG
YUE WANG
Beihang University, Beijing, China

By applying the bilinear-tangent (BLT) guidance law, a near-optimal and computationally efficient BLT constant-thrust guidance (BCG) algorithm is introduced for orbital transfers about a binary asteroid system. This algorithm is accomplished by using the BLT guidance law combined with the Newton–Raphson predictor–corrector algorithm and manifold patching techniques. BCG can plan a variety of fuel efficient constant-thrust state/orbit to state/orbit transfers based on the types of the initial/target orbits and the selected maneuver types, including single-burn transfers and multiple-burn transfers leveraging manifolds. For the study case of 66391 Moshup, a 600-kg, BCG-guided spacecraft with a 24-mN thruster performed an aggressive noncoplanar transfer between L1 and L2 Halo orbits at the cost of only 3.38 g of fuel. Then, the BCG-guided trajectories' robustness is validated thoroughly by $N = 600$ Monte Carlo simulations, respectively. Finally, BCG's excellent tradeoff between computational efficiency and near-optimality is well demonstrated by comparison with well-established optimization methods. For example, in a coplanar transfer with a 1.5-mN thruster, BCG can converge over 200 times faster than interior point optimization with only a 9% cost surplus in fuel compared to the optimum. It is indicated that the BCG algorithm is a promising option for autonomous orbital control in binary asteroid missions considering its computational and fuel efficiency.

Manuscript received 1 August 2023; revised 5 December 2023; accepted 19 February 2024. Date of publication 23 February 2024; date of current version 9 August 2024.

DOI. No. 10.1109/TAES.2024.3369005

Refereeing of this contribution was handled by Marcello Romano.

This work was supported by the National Natural Science Foundation of China under Grant 11872007.

Authors' addresses: Zicen Xiong and Yue Wang are with the School of Astronautics, Beihang University, Beijing 102206, China, E-mail: (xiongzicen@buaa.edu.c; ywang@buaa.edu.cn). *(Corresponding author: Yue Wang.)*

I. INTRODUCTION

In recent decades, binary asteroid systems have been receiving increasing interest in terms of planetary science and resource utilization. Several missions have been or are going to be launched to binary asteroid systems, such as NASA's Lucy flyby mission to Trojan binary asteroids 3458 Eurybates and 617 Patroclus [1] and the Asteroid Impact and Deflection Assessment missions heading to asteroid 65803 Didymos, consisting of NASA's Double Asteroid Redirection Test (DART) mission and ESA's Hera mission [2], [3].

Hitherto, most of the deep space missions are propelled by chemical thrusters when executing maneuvers, such as the ones Lucy is equipped with, whose maximum specific impulse is only 324 s [4]. Meanwhile, chemical thrust is so strong that the proportional errors would be driven larger when executing finer maneuvers in the weaker gravitational fields near binary asteroids because of the extremely short burns [5]. In contrast, the electric propulsion system is an ideal choice for deep space and long-term asteroid missions thanks to its high specific impulse of over 1000–10 000 s and a thrust ranging from 0.1 mN to 50 N, enabling longer and more versatile missions [6].

Current missions with low-thrust electric propulsion heading toward asteroids are either simple flybys like DeepSpace-1 [7] or direct impact like DART [2]. Another type is Hayabusa and Hayabusa2, which were equipped with ion thrusters for heliocentric cruising but later switched to a bipropellant hydrazine system after rendezvousing with asteroids [8], [9]. In these missions, the communication difficulties to the ground-based control (e.g., minute-level latency, bandwidth limits, etc.), time-critical decisions, and maneuvers about the asteroids were devised by the spacecraft's real-time autonomous guidance navigation and control (GNC). Despite their success, these missions only orbited or contended with the complex dynamical environment about asteroids quite fleetingly, and then, cruised heliocentrically, forsaking the potential of electric propulsion systems in fuel efficiency and precision in flight control. On the contrary, with respect to the binary asteroid missions involving probably extended mission durations and more arduous operations (e.g., close-range orbital transfers, multiple proximities, station-keeping maneuvers, etc.) in more perturbed dynamical systems, electric propulsion systems will become increasingly indispensable.

Thus, the autonomous and computationally efficient GNC for low-thrust propulsion systems (e.g., autonomous orbit determination, starlight navigation, autonomous guidance algorithms, etc.) is required to perform the time-critical maneuvers with real-time in situ data directly obtained and processed by onboard sensors and computers. This article will be focused on autonomous algorithms for the transfer trajectory design.

The most common approaches for solving optimal low-thrust trajectory can be divided into three categories: indirect approaches relying on Pontryagin's minimum principle, direct approaches on Karush–Kuhn–Tucker conditions,

and dynamic programming [10], [11], involving techniques like collocation methods [12], [13], [14], single-shooting or multiple-shooting methods [15], [16]. From a more specified perspective in the circular restricted three-body problem (CR3BP), the low-thrust trajectory optimal design algorithms include indirect shooting [17], [18], [19], [20]; machine-learning-based shooting [21]; direct collocation methods [22]; direct collocation and attainable sets methods using manifolds [23], [24]; direct successive convex optimization [25]; particle swarm optimization method [26]; finite Fourier series [27]; some other initial guess solving methods leveraging the structure of dynamical systems [28], etc. The aforementioned low-thrust optimization algorithms are mostly restricted to the cislunar environment where the initial orbits are normally geostationary transfer orbit, geostationary orbit, or distant retrograde orbit far from the celestial bodies without a pressing need for time-critical reactions. As such, they are too computationally expensive and time inefficient for onboard computers. Hence, there is a lacuna in computational efficient algorithms for autonomous constant low-thrust guidance about binary asteroid systems.

This article introduces a fuel-efficient bilinear-tangent (BLT) constant-thrust guidance (BCG) algorithm, which is capable of planning transfers about a binary asteroid system inspired by Kuttel and McMahon's BLT low-thrust maneuver in the perturbed two-body environment [29]. The BCG algorithm applies the BLT guidance law to the binary asteroid systems, leveraging manifolds and Newton–Raphson predictor–corrector (NRPC) methods to design constant low-thrust trajectories, with near optimality and high computational efficiency.

The rest of this article is organized as follows. In Section II, the binary asteroid system is introduced. In Section III, the low-thrust trajectory optimization problem and the structure of the BCG algorithm are examined in detail, including the initial guess and convergence stages. In Section IV, BCG's maneuver planning capability was demonstrated with several transfers. In Section V, a multitude of numerical simulations were performed to provide an insight into the algorithm's robustness; the tradeoff between computational efficiency and optimality of BCG is determined by comparing it with a well-established optimizer. In Section VI, the results are further discussed. Finally, Section VII concludes this article.

II. BACKGROUND

The binary asteroid 66391 Moshup is chosen as the study case. This section will first introduce the facts about the binary asteroid system and spacecraft's equations of motion are then constructed based on the CR3BP.

A. Dynamical Environment of 66391 Moshup

The 66391 Moshup is an Aten asteroid, classified as a potentially hazardous asteroid by researchers [30]. The binary system consists of a primary and a secondary (seen in Table I).

TABLE I
Facts About 66391 Moshup [31]

66391 Moshup	Primary (Alpha)	Secondary (Beta)
Mass [10^{12} kg]	2.353	0.135
Density [$\mathrm{kg}\cdot m^{-3}$]	1970	2810
Radius [m]	~500	~100
Period [h]	17.4223	
Barycenter dist. [m]	2550	

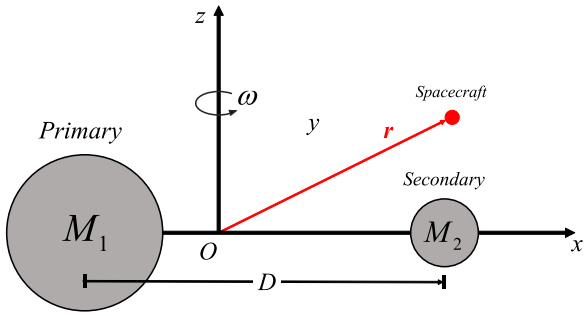

Fig. 1. Synodic frame of a binary asteroid system.

B. Linear Relative Motion Dynamics

A massless spacecraft moving in the gravity field of a binary asteroid system is considered. As shown in Fig. 1, M_1 and M_2 are the masses of the primary and secondary of the binary system, respectively, and D is the relative position separation of the secondary with respect to the primary.

The mass ratio of the binary system is defined as

$$\mu = \frac{M_2}{M_1 + M_2}. \tag{1}$$

The mutual motion of the binary is assumed to be circular with a constant angular velocityω. The barycenter of the binary and the mutual orbital plane are assumed to be stationary in the inertial frame. A synodic frame with angular velocity ω is defined with its origin located at the barycenter, with the x-axis pointing to the barycenter of secondary, and the $x-y$ plane within the mutual orbital plane. The primary and secondary of 66391 Moshup are assumed to be in in a doubly synchronous state. This is what Moshup's relaxed mode would be if the secondary were tidally despun to a synchronous rotation rate [31]. $\mathbf{r}$ is the position vector of the spacecraft in the synodic frame.

Then, the spacecraft's equations of motion in the synodic frame are obtained [32]

$$\boldsymbol{r} = \begin{bmatrix} x & y & z \end{bmatrix}^T \tag{2}$$

$$\dot{\boldsymbol{r}} = \begin{bmatrix} \dot{x} & \dot{y} & \dot{z} \end{bmatrix}^T \tag{3}$$

$$\ddot{\boldsymbol{r}} = f(\dot{\boldsymbol{r}}, \boldsymbol{r}, U) = \begin{bmatrix} \frac{\partial U}{\partial x} + 2\omega\dot{y} + \omega^2 x \\ \frac{\partial U}{\partial y} - 2\omega\dot{x} + \omega^2 y \\ \frac{\partial U}{\partial z} \end{bmatrix} \tag{4}$$

where U is the force potential of the system. In addition, (4) admits an integral, known as C_j, Jacobian integral or Jacobi constant, defined as [33]

$$\frac{1}{2}C_j = -\frac{1}{2}\left(\dot{x}^2+\dot{y}^2+\dot{z}^2\right)+\frac{1}{2}\omega^2\left(x^2+y^2\right)+U(\boldsymbol{r}). \quad (5)$$

Using this equation and setting the velocity terms of (5) to be 0, the zero velocity curve (ZVC) for the three-body problem is obtained and separates the coordinates into three realms: the realm of the primary (P), the realm of the secondary (S), and the exterior realm outside the ZVC.

1) *Spacecraft's Motion in the Simplified Model:* Since a point-mass model will significantly distort the dynamic structures and the topology of the actual orbits, this article uses the spherical harmonic model in the initial guess stage (see Section III-C) for its relatively precise and closed-form gravity, which promises computational efficiency. U_{sh} is the force potential of spherical harmonic gravity [34]

$$U_{\text{sh}}(\boldsymbol{r}) = U^1_{\text{sh}}(\boldsymbol{r}+\mu\boldsymbol{d})+U^2_{\text{sh}}[\boldsymbol{r}-(1-\mu)\boldsymbol{d}] \quad (6)$$

$$U^i_{\text{sh}}(\boldsymbol{r}_i) = -\frac{GM_i}{r_i}\sum_{l=0}^{\infty}\sum_{m=0}^{l}\left(\frac{R^i_0}{r_i}\right)^l P_{lm}(\sin\delta_i)(C_{lm}\cos m\lambda_i + S_{lm}\sin m\lambda_i) \quad i=1,2 \quad (7)$$

where G is the gravitational constant; M_i is the asteroid mass; R^i_0 is the normalizing radius of the asteroid;$P_{lm}$is the associated Legendre function; C_{lm} and S_{lm} are the spherical harmonic gravity coefficients; and r_i,δ_i, and λ_i are the radius, latitude, and longitude coordinates of spacecraft's position (i.e.,$\boldsymbol{r}+\mu\boldsymbol{d}$ and $\boldsymbol{r}-(1-\mu)\boldsymbol{d}$ in the asteroid fixed frames), respectively. Subscripts 1 and 2 refer to the primary and the secondary, respectively.

2) *Spacecraft's Motion in Realistic Model:* In the convergence stage of the algorithm (see Section III-D), a more realistic model is employed. The relaxed mode of the binary asteroid system at aphelion, 1.622×10^8 km(1.1 AU) from the Sun, is considered [35].

At this distance, the majority of the perturbations on the binary system are solar radiation pressure and solar third-body perturbation, while the heliocentric orbital inclination of the binary asteroids and perturbations from other planets is ignored.

Constant-thrust equations of motion of the spacecraft in the synodic frame are defined as

$$\ddot{\boldsymbol{r}} = f\left(\dot{\boldsymbol{r}},\boldsymbol{r},U_{\text{poly}}\right)+\frac{F}{m_0-g_0I_{\text{sp}}t}\hat{\boldsymbol{u}}+\ddot{\boldsymbol{r}}_{\text{srp}}+\ddot{\boldsymbol{r}}_{\odot\text{TB}} \quad (8)$$

$$\ddot{\boldsymbol{r}}_{\text{srp}} = p_{\text{SR}}A_{\text{sc}}C_R\frac{\boldsymbol{r}_{\odot,\text{sc}}}{\left|\boldsymbol{r}_{\odot,\text{sc}}\right|} \quad (9)$$

$$\ddot{\boldsymbol{r}}_{\odot\text{TB}} = \mu_\odot\left[-\frac{\boldsymbol{r}_{\odot,\text{sc}}}{\left|\boldsymbol{r}_{\odot,\text{sc}}\right|^3}+\frac{\boldsymbol{r}_{\odot,\text{Mo}}}{\left|\boldsymbol{r}_{\odot,\text{Mo}}\right|^3}\right] \quad (10)$$

F is the magnitude of thrust, $\hat{\boldsymbol{u}}$ is thrust vector, m_0 is spacecraft mass, I_{sp} is specific impulse, g_0 is standard gravitational constant, $\ddot{\boldsymbol{r}}_{\text{srp}}$ is acceleration contributed by cannonball-modeled solar radiation pressure, p_{SR} is solar radiation pressure at 1.1 AU, A_{sc} is the spacecraft's solar projected area, C_R is the spacecraft's equivalent reflectivity to solar radiation, $\ddot{\boldsymbol{r}}_{\odot\text{TB}}$ is solar third-body perturbations, $\mu_\odot$is the solar gravitational constant, $\boldsymbol{r}_{\odot,\text{sc}}$ is the position vector from the sun to the spacecraft, and $\boldsymbol{r}_{\odot,\text{Mo}}$ is the position vector from the sun to the barycenter of 66391 Moshup [36]. And U_{poly} is the force potential of polyhedron-modeled gravity [33], [37]

$$U_{\text{poly}} = U^1_{\text{poly}}(\boldsymbol{r}+\mu\boldsymbol{d})+U^2_{\text{poly}}[\boldsymbol{r}-(1-\mu)\boldsymbol{d}] \quad (11)$$

$$U^i_{\text{poly}}(\boldsymbol{r}_i) = \tfrac{1}{2}G\sigma\left(\sum_{e\in\text{edges}}L_e\boldsymbol{r}^T_{ie}E_{ie}\boldsymbol{r}_{ie}-\sum_{f\in\text{faces}}\omega_f\boldsymbol{r}^T_{if}F_{if}\boldsymbol{r}_{if}\right) \quad i=1,2 \quad (12)$$

where σ_i is the density of the asteroid, $L_e$is an integration factor of the spacecraft's position and the edge, ω_{if} is the solid angle of the face relative to the spacecraft, E_{ie} and F_{if} are geometric parameters of edges and faces, respectively, and $\boldsymbol{r}_{ie}$ and $\boldsymbol{r}_{if}$are body-fixed vectors from the spacecraft to the edge and the face of the polyhedron, respectively. The remainder symbols correspond with the ones in (7).

In the following sections, unless otherwise specified, the spacecraft's motion is calculated in a synodic frame with normalized units. This is done for the sake of computational convenience and to ensure the stability of numerical methods. Length and time are normalized by the system's characteristic length and period, as shown in Table I, as follows:

$$\bar{\boldsymbol{r}} = \frac{\boldsymbol{r}}{D_{\text{Moshup}}},\quad \bar{t} = \frac{2\pi t}{T_{o,\text{Moshup}}},\quad \bar{\omega}_a = 1. \quad (13)$$

III. BCG ALGORITHM

The BLT guidance law functions as the underlying algorithm throughout the BCG-guided trajectories. This section will first give the derivation of the BLT law, and then, examine the structure of the BCG algorithm explicitly, including the initial guess stage and the convergence stage.

A. BLT Guidance

The BLT functions as the underlying algorithm of the initial guess and convergence stages throughout the guidance.

Traditionally, the optimal control for the continuous-thrust spacecraft is an infinite-dimensional optimization problem, which requires some computationally onerous nonlinear optimizers (as in [11], [12], [13], [14], [15], [16], [17], [18], [19], [20], [21], [22], [23], [24], [25], [26], [27], and [28]) to obtain the true optimal control. To overcome the dilemma of onboard computation efficiency, this algorithm employs BLT guidance, which was traditionally applied to solid-propellant rocket guidance in a planar gravitational field. It is a time-optimal guidance law, namely fuel-optimized for constant-thrust engines. The equations of motion of a spacecraft are

$$\dot{\boldsymbol{x}} = \begin{bmatrix}\dot{\boldsymbol{r}}\\ \dot{\boldsymbol{v}}\end{bmatrix} = \begin{bmatrix}\boldsymbol{v}\\ \boldsymbol{g}(\boldsymbol{r},t)+\frac{F}{m}\boldsymbol{u}\end{bmatrix} \quad (14)$$

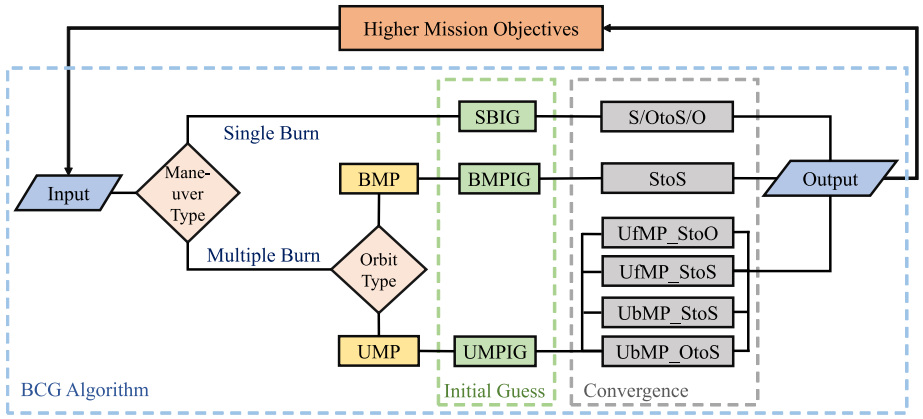

Abbr.: SBIG: Single burn initial guess
BMP: Bilateral manifold patching
UMP: Unilateral manifold patching
UfMP: Unilateral forward manifold patching
UbMP: Unilateral backward manifold patching
S/OtoS/O: State/Orbit elements to State/Orbit elements
BMPIG: BMP initial guess
UMPIG: UMP initial guess

Fig. 2. Flowchart of the BCG algorithm in CR3BP.

where $\boldsymbol{r}$ is the position vector of the spacecraft in the synodic frame, $\boldsymbol{v}$ is the velocity of the spacecraft, m is the mass of the spacecraft, F is the force of the constant-thrust, $\boldsymbol{u}$ is a unit vector in the direction of the thrust acceleration, and $\boldsymbol{g}$ is the given gravitational field.

When minimizing the flight time, the variational Hamiltonian is written as [38]

$$H = L(t,\boldsymbol{x},\boldsymbol{u}) + \boldsymbol{\lambda}^T f(t,\boldsymbol{x},\boldsymbol{u}) = \begin{bmatrix} \boldsymbol{\lambda}_r \\ \boldsymbol{\lambda}_v \end{bmatrix}^T \begin{bmatrix} \boldsymbol{v} \\ g(\boldsymbol{r},t) + \frac{F}{m}\boldsymbol{u} \end{bmatrix} - 1. \tag{15}$$

And its costate equations

$$\dot{\boldsymbol{\lambda}}_r = -\frac{\partial \boldsymbol{H}}{\partial \boldsymbol{r}} = -\boldsymbol{\lambda}_v{}^T \left[\frac{\partial \boldsymbol{g}(\boldsymbol{r},t)}{\partial \boldsymbol{r}}\right] \tag{16}$$

$$\dot{\boldsymbol{\lambda}}_v = -\frac{\partial \boldsymbol{H}}{\partial \boldsymbol{v}} = -\boldsymbol{\lambda}_r. \tag{17}$$

Differentiating (16) with respect to time and substituting (17) yields

$$\ddot{\boldsymbol{\lambda}}_v = \boldsymbol{\lambda}_v{}^T \left[\frac{\partial \boldsymbol{g}(\boldsymbol{r},t)}{\partial \boldsymbol{r}}\right]. \tag{18}$$

The time optimal control is achieved by applying Pontryagin's principle to (15). The optimal $\boldsymbol{u}$ is chosen to be antiparallel to $\boldsymbol{\lambda}_v$as follows:

$$\boldsymbol{u}^* = -\frac{\boldsymbol{\lambda}_v}{\lambda_v}. \tag{19}$$

In the case of a planar gravitational field, $\boldsymbol{g}(\boldsymbol{r},t)$ equals a constant so that

$$\ddot{\boldsymbol{\lambda}}_v = 0. \tag{20}$$

Integrating twice gives the vector linear equations

$$\boldsymbol{\lambda}_v = \boldsymbol{A} + \boldsymbol{B}t \tag{21}$$

where $\boldsymbol{A}$ and $\boldsymbol{B}$ are constant vectors of integration. Substituting these into (19) gives the time-optimal thrust pointing direction

$$\widehat{\boldsymbol{u}} = \frac{\boldsymbol{A} + \boldsymbol{B}t}{|\boldsymbol{A} + \boldsymbol{B}t|} \tag{22}$$

where$\widehat{\boldsymbol{u}} \in \boldsymbol{R}^3$, $\boldsymbol{A} \in \boldsymbol{R}^3$, and $\boldsymbol{B} \in \boldsymbol{R}^3$ are the thrust direction and BLT control profiles, and t is the time duration since the maneuver starting epoch.

B. Description of the Algorithmic Flow

Fig. 2 shows the main execution flowchart of BCG. In the initial guess stage, guided by higher mission objectives (e.g., close-range observation and collision avoidance), BCG plans nominal impulsive maneuvers of different types (single burn and multiple burns based on manifold patching) by leveraging the invariant manifolds of CR3BP. With the initial guess, the spacecraft performs transfer maneuvers according to the selected orbits' types (state-to-state, orbital element-to-state, state-to-orbital element). During the convergence stage, the BCG algorithm continuously updates the guidance parameters to correct errors caused by the discrepancy between the actual gravity field and the loaded gravity field onboard the spacecraft.

From an overview perspective, BCG first finds the optimal impulsive-like maneuver control within constraints, and then, converts it into BLT control parameters. This algorithm is used to design BLT transfers in versatile scenarios. The specific definitions of these transfer scenarios are as follows.

1) Single burn, the basic form of BLT guidance, which can transfer between any initial and target orbits with thrusters on all the way.

2) Multiple burns, which plan multiple BLT thrust burn segments and free coasting (with thrusters OFF) segments to accomplish transfers.
3) Bilateral manifold patching (BMP), a category of multiple burns that is specified for scenarios in CR3BP when both the target and initial orbits have invariant manifolds (i.e., Lyapunov orbit families near the collinear libration points, and the halo orbit families).
4) Unilateral manifold patching (UMP), another category of multiple burns when one of the initial/target orbits is stable and does not generate any invariant manifold, and the other is a libration point periodic orbit which has manifolds.

For the single-burn maneuver, as shown in Fig. 4, its transfer scenarios include six states to six states (StoS, i.e., two 6-D states involving position and velocity vectors), six states to five orbit elements (StoO, i.e., classical orbital elements except for true anomaly), five orbit elements to six states (OtoS), and five or $\boldsymbol{u}^* = -\frac{\boldsymbol{\lambda}_v}{\lambda_v}$ bit elements to five orbit elements (OtoO). It should be noted that the perturbed two-body orbits must be the target orbit of StoO, both the initial and target orbits of OtoO and the initial orbit of OtoS, whose equations of motion can be expressed in terms of orbital elements with respect to the barycenter of 66391 Moshup.

For multiple-burn maneuvers, two categories of maneuvers can be distinguished based on differences in manifold propagation: BMP involves only StoS since the transfer between orbits with invariant manifolds is hard to parameterize with orbital elements; in the context of UMP, when the initial orbit generates manifolds, the scenario is called unilateral forward manifold patching (UfMP) including StoO and StoS, and when the target orbit generates manifolds, it is called unilateral backward manifold patching (UbMP) including StoS and OtoS.

On the whole, BCG is divided into the initial guess stage and the convergence stage, which are, respectively, carried out under spherical harmonics (seen in Section II-B1) and more realistic gravitational fields (seen in Section II-B2). The single-burn initial guess (SBIG) algorithm is used for a single burn. Multiple-burn initial guess (MBIG) is divided into bilateral manifold patching initial guess (BMPIG) and unilateral manifold patching initial guess (UMPIG).

C. Initial Guess Stage Under Spherical-Harmonic Gravity

The parameters solved by the initial guess stage include the BLT control profiles in (22) and initial and target states. These coarse targeting methods solve the initial guess to meet a specific optimal goal. This part will describe the mathematics of the optimization problem.

1) *Single-Burn Initial Guess (SBIG):* Single burn of BCG will be focused on transfers between some special orbits of CR3BP (i.e., Lyapunov and Halo orbits), since the optimization problems for transfers under the perturbed two-body problem have been well established in Kuttel's work [39]. It should be noted that the orbits associated with libration points are hard to derive in closed forms, which means the freedom of variables associated with the orbital phase cannot be released as orbital elements are, so the StoS single burn is emphasized in CR3BP. However, a pseudo-OtoO can be achieved by adjusting departure and arrival points on the initial and target orbits through orbital propagation with designated epochs. Then, a complete SBIG is separated into two parts: 1) solving BLT parameters and 2) phase adjusting.

To optimize the time of flight, the closest points (in the 6-D state space) on the initial and target orbits are searched and chosen to derive the BLT parameters. For the generality of the objective function, all the phase-related variables on the orbits are transcribed into state-time forms (an arbitrary state $\boldsymbol{x}$ and orbital propagation with a designated duration t from $\boldsymbol{x}$) in the following optimization problems in (23)–(56).

The following equations describe the optimization problem:

$$\boldsymbol{x}_t^* = f\left(t_t^*, \boldsymbol{x}_t^0\right), \boldsymbol{x}_i^* = f\left(t_i^*, \boldsymbol{x}_i^0\right) \tag{23}$$

$$t_t^*, t_i^* = \underset{t_t \quad t_i}{\arg\min} \left[\Delta \boldsymbol{x}_{\mathrm{BLT}}(t_t, t_i)^T \Delta \boldsymbol{x}_{\mathrm{BLT}}(t_t, t_i)\right] \tag{24}$$

$$\Delta \boldsymbol{x}_{\mathrm{BLT}} = \boldsymbol{x}_t\left(t_t, \boldsymbol{x}_t^0\right) - \boldsymbol{x}_i\left(t_i, \boldsymbol{x}_i^0\right) \tag{25}$$

where f is the equation of motion, subscripts i and t denote variables on the initial and target orbits, respectively, $\boldsymbol{x}_t^0$ and $\boldsymbol{x}_i^0$ are the arbitrarily selected initial states, and t_t and t_i are time of orbital propagation from the starting states $\boldsymbol{x}_t^0$ and $\boldsymbol{x}_i^0$ to the objective states $\boldsymbol{x}_t$ and $\boldsymbol{x}_i$. By applying the Broyden–Fletcher–Goldfarb–Shanno (BFGS) algorithm to the unconstrained optimization, SBIG can be solved. It is an efficient quasi-Newton method, which avoids gradient solving and ensures rapid convergence [40, pp. 136–149]. The solved $\Delta \boldsymbol{x}_{\mathrm{BLT}}^*$ will be converted into BLT control according to the following equations:

$$T = \sqrt{\frac{2\left|\Delta \boldsymbol{r}^*\right|}{a_{\mathrm{th}}}} \tag{26}$$

$$\boldsymbol{A} = \frac{\Delta \boldsymbol{r}^*}{\left|\Delta \boldsymbol{r}^*\right|} \tag{27}$$

$$\boldsymbol{B} = \frac{\Delta \boldsymbol{v}^*}{\left|\Delta \boldsymbol{v}^*\right|} - \frac{\Delta \boldsymbol{r}^*}{\left|\Delta \boldsymbol{r}^*\right| T} \tag{28}$$

where $\Delta \boldsymbol{r}^*$ and $\Delta \boldsymbol{v}^*$ are the position and velocity components of the closest state separation $\Delta \boldsymbol{x}_{\mathrm{BLT}}^*$, respectively, a_{th} is the acceleration magnitude and T is an approximate flight time for performing BLT maneuver, $\boldsymbol{A}$ is defined by $\Delta \boldsymbol{r}^*$ to constrain the departure direction to the target, and use $\Delta \boldsymbol{r}^*$ and $\Delta \boldsymbol{v}^*$ to define B, associated with T so that the control vector will tend to the target state's velocity components at the terminal of flight. The states obtained in (24) were only to provide initial guess for guidance parameters instead of being the real departure/arrival states, for its destined miss of target orbits as shown in Fig. 3.

The departure/arrival states for each specified thrust level require further determination. Therefore, SBIG again

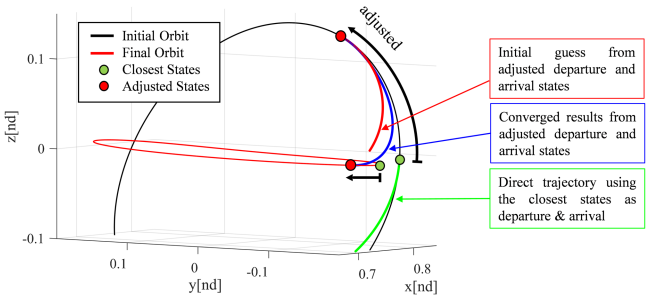

Fig. 3. Phase adjustment for SBIG.

takes the departure and arrival states as variables, and the objective function is the two-norm of the state errors between the predicted arrival state and the target state on target orbit. The search for adjusted states on the initial/target orbits is indefinite and the temporal parameters can be either positive or negative according to the orbital geometry. The modified optimization problem parameters are described as follows:

$$\begin{aligned} &\boldsymbol{x}_{t,m}^{*}=f\left(\Delta t_{t,m}^{*}, \boldsymbol{x}_{t}^{*}\right), \boldsymbol{x}_{i,m}^{*}=f\left(\Delta t_{i,m}^{*}, \boldsymbol{x}_{i}^{*}\right) \\ &\boldsymbol{x}_{\mathrm{arr},m}^{*}=f_{\mathrm{burn}}\left(\boldsymbol{x}_{i,m}^{*}, \boldsymbol{A}, \boldsymbol{B}, T\right) \end{aligned} \tag{29}$$

$$\begin{aligned} &\Delta t_{t,m}^{*}, \Delta t_{i,m}^{*} \\ &\quad=\underset{t_{t,m} \quad t_{i,m}}{\arg\min}\left[\Delta \boldsymbol{x}_{m}\left(\Delta t_{t,m}, \Delta t_{i,m}\right)^{T} \Delta \boldsymbol{x}_{m}\left(\Delta t_{t,m}, \Delta t_{i,m}\right)\right] \end{aligned} \tag{30}$$

$$\Delta \boldsymbol{x}_{m}=\boldsymbol{x}_{t,m}-\boldsymbol{x}_{\mathrm{arr},m} \tag{31}$$

where f_{burn} is the equation of motion with thrusters on, $\Delta t_{i,m}$ and $\Delta t_{t,m}$are time of orbital propagation from the closest states $\boldsymbol{x}_{t}^{*}$ and $\boldsymbol{x}_{i}^{*}$ from (23), $\boldsymbol{x}_{i,m}$ and $\boldsymbol{x}_{t,m}$ are the objective phase-modified initial and target state, and $\boldsymbol{x}_{\mathrm{arr},m}$ is the predicted arrival state when using current BLT profiles to transfer from $\boldsymbol{x}_{i,m}$.

As such, the pseudo-OtoO is achieved by orbital propagation. This problem can be solved by BFGS as well. As illustrated in Fig. 3, the phase-adjusted initial guess still does not necessarily reach the target state, however, it results in a solution that is good enough to be used in the convergence step, which follows.

2) *MBIG Leveraging Manifolds:* Due to the strong dynamical drift in a binary asteroid system, it is not economical to use transfers implementing Lambert maneuvers and a precarious way involves a high probability of impact. In contrast, MBIG yields the initial impulsive maneuver by leveraging the stable and unstable manifolds of the orbits in CR3BP.

Stable and unstable manifolds start from the perturbed initial vector associated with the stable or unstable eigenvectors $\boldsymbol{w}_{s}$ and $\boldsymbol{w}_{u}$ of the monodromy of periodic orbits. The monodromy matrix $\boldsymbol{M}$ of the periodic orbit is defined as [41]

$$\boldsymbol{M}=\boldsymbol{\Phi}(T, 0)=I_{6\times 6}+\int_{0}^{T} \boldsymbol{\Gamma}(t) \boldsymbol{\Phi}(t, 0) dt \tag{32}$$

$$\boldsymbol{\Gamma}(t)=\frac{\partial f(X)}{\partial X}(t)$$

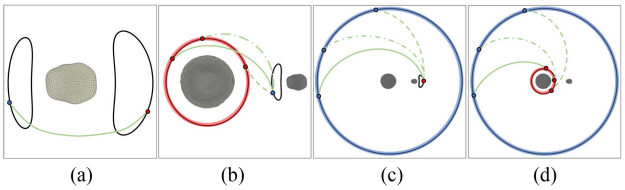

Fig. 4. Different transfer types: red for target orbits/states, and blue for initial orbits/states.

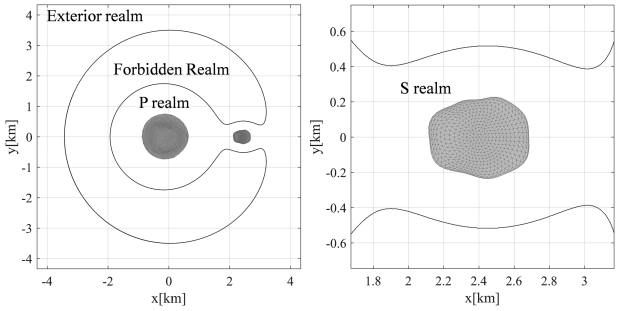

Fig. 5. *P*, *S*, and exterior realm near 66391 moshup.

$$=\begin{bmatrix} 0 & 0 & 0 & 1 & 0 & 0 \\ 0 & 0 & 0 & 0 & 1 & 0 \\ 0 & 0 & 0 & 0 & 0 & 1 \\ \omega^{2}+U_{xx} & U_{xy} & U_{xz} & 0 & 2\omega_{a} & 0 \\ U_{yx} & \omega^{2}+U_{yy} & U_{yz} & -2\omega_{a} & 0 & 0 \\ U_{zx} & U_{zy} & \omega_{a}^{2}+U_{zz} & 0 & 0 & 0 \end{bmatrix} \tag{33}$$

where T denotes the orbital period, $I_{6\times 6}$ is an identity matrix, $\boldsymbol{\Phi}(T, 0)$ is the state transition matrix, $\boldsymbol{\Gamma}(t)$ is the Jacobian matrix, $f(X)$ is the equation of motion in CR3BP, and U_{ij} are the partial derivatives of the force potential. The stable and unstable eigenvalue of $\boldsymbol{M}$ are $\lambda_{s}<1$ and $\lambda_{u}=1/\lambda_{s}$, while the corresponding eigenvector is $\boldsymbol{w}_{s}$ and $\boldsymbol{w}_{u}$. The initial state of a manifold can be generated by adding marginal deviation d (generally, 10^{-6} is adopted) along the eigenvector [42] to the periodic states $\boldsymbol{x}_{0}$ as

$$\begin{aligned} \boldsymbol{x}_{s}&=\boldsymbol{x}_{0} \pm d \cdot \boldsymbol{w}_{s} \\ \boldsymbol{x}_{u}&=\boldsymbol{x}_{0} \pm d \cdot \boldsymbol{w}_{u}. \end{aligned} \tag{34}$$

Then, the stable manifold W^{s} is backward propagated from $\boldsymbol{x}_{s}$ and the unstable manifold W^{u} is forward propagated from $\boldsymbol{x}_{u}$. The sign determines which realm the manifold will lead to. For interpretation, taking L1 Lyapunov orbits of 66391 Moshup as an example, positive $\boldsymbol{x}_{s}^{+}$generates manifold $W_{L_1}^{s,P}$ in the P (primary asteroid) realm, while negative $\boldsymbol{x}_{s}^{-}$ generates $W_{L_1}^{s,S}$in the S (secondary asteroid) realm shown in Fig. 5. In BMP and UMP, only the velocity component of deviation (eigenvector) is considered in (34) to generate manifolds

$$\begin{aligned} \boldsymbol{x}_{s}&=\boldsymbol{x}_{0} \pm d \cdot \boldsymbol{v}_{s} \\ \boldsymbol{x}_{u}&=\boldsymbol{x}_{0} \pm d \cdot \boldsymbol{v}_{u}. \end{aligned} \tag{35}$$

MBIG selects different patching cuts/hyperplanes according to the type of transfer orbit (UMP or BMP) and

the nature of the orbit to reduce the degree of freedom of the nonlinear optimization problem. Nevertheless, this method still requires orbits to have intersected invariant manifolds from both ends. The two initial guess algorithms are described follows.

1) BMPIG involves initial and target orbits associated with equilibriums, both of which generate invariant manifolds and the corresponding deviations are chosen as BMP's impulsive guess. Specifically, the unstable/stable manifolds from the designated state on the initial/target orbit are forward/backward propagated and are patched on some selected hyperplanes like Poincaré cuts (such as $x = 1 - \mu$ or $x = -\mu$) in the synodic frame where the third impulsive burn will be executed.

The BMPIG optimization problem is exemplified by using the denotation of the transfer from L1 to L2. To make the two manifolds intersect, it is necessary to compensate for the C_j gap by altering the C_j energy of each manifold W, allowing them to propagate within the S realms of a congenial size, reducing state discrepancies when intersecting. The unstable manifold of L1 in S realm, $W_{L_1}^{u,S}$, the stable manifold of L2 in S realm, $W_{L_2}^{s,S}$, and $\boldsymbol{\Sigma} : x = 1 - \mu$ as the patching cuts are selected as an example. Since it is almost impossible to generate two identical states on the cuts from two arbitrary orbits, the state discrepancy on the $y - z$ plane is chosen to be the least. Since manifolds are required on both ends, BMPIG only involves StoS [states are required to calculate the monodromy in (32)].

Recall that pseudo-OtoO is achieved by SBIG in (29), BMPIG does so as well. Then, the free variables are the deviations in (34):d_{L_1} and d_{L_2}, and the phase variables on L1/L2: t_{L_1} and t_{L_2}. The objective function is the sum of the two-norm of $\Delta \boldsymbol{v}^*$ and C_j gap. Distinguished from SBIG, BMPIG solves a constrained optimization problem with a constraint placed on manifolds' position difference at the cut $\boldsymbol{\Sigma}$as follows:

$$
\begin{aligned}
\boldsymbol{x}_{L_1}^* &= f\left(t_{L_1}^*, \boldsymbol{x}_{L_1}^0\right) \\
\boldsymbol{x}_{L_2}^* &= f\left(t_{L_2}^*, \boldsymbol{x}_{L_2}^0\right) \\
\Delta \boldsymbol{v}_{L_1}^* &= d_{L_1}^* \cdot v\left(\boldsymbol{w}_{L_1}^u\left(\boldsymbol{x}_{L_1}^*\right)\right) \\
\Delta \boldsymbol{v}_{L_2}^* &= d_{L_2}^* \cdot v\left(\boldsymbol{w}_{L_2}^s\left(\boldsymbol{x}_{L_2}^*\right)\right) \\
\Delta \boldsymbol{v}_{\boldsymbol{\Sigma}}^* &= \boldsymbol{v}_{\boldsymbol{\Sigma},L_2}\left(\boldsymbol{\Sigma}, W_{L_2}^{s,S}\left(d_{L_2}^*, \boldsymbol{x}_{L_2}^*\right)\right) \\
&\quad - \boldsymbol{v}_{\boldsymbol{\Sigma},L_1}\left(\boldsymbol{\Sigma}, W_{L_1}^{u,S}\left(d_{L_1}^*, \boldsymbol{x}_{L_1}^*\right)\right) \qquad (36) \\
&\text{StoS(pseudo} - \text{OtoO)} : t_{L_1}^*, d_{L_1}^*, t_{L_2}^*, d_{L_2}^* \\
&= \underset{t_{L_1}, d_{L_1}, t_{L_2}, d_{L_2}}{\arg\min} \left[\Delta \boldsymbol{v}_{L_1}{}^T\left(t_{L_1}, d_{L_1}\right) \Delta \boldsymbol{v}_{L_1}\left(t_{L_1}, d_{L_1}\right)\right. \\
&\quad + \Delta \boldsymbol{v}_{L_2}{}^T\left(t_{L_2}, d_{L_2}\right) \Delta \boldsymbol{v}_{L_2}\left(t_{L_2}, d_{L_2}\right) \\
&\quad \left. + \left|\Delta C_j\left(t_{L_1}, d_{L_1}, t_{L_2}, d_{L_2}\right)\right|\right] \\
&\quad \text{s.t.} \quad \left|\Delta \boldsymbol{r}_{\boldsymbol{\Sigma}}\left(t_{L_1}, d_{L_1}, t_{L_2}, d_{L_2}\right)\right| = 0 \qquad (37) \\
\Delta C_j &= C_j\left(W_{L_2}^{s,S}\left(d_{L_2}, \boldsymbol{x}_{L_2}\right)\right) - C_j\left(W_{L_1}^{u,S}\left(d_{L_1}, \boldsymbol{x}_{L_1}\right)\right) \qquad (38) \\
\Delta \boldsymbol{r}_{\boldsymbol{\Sigma}} &= \boldsymbol{r}_{\boldsymbol{\Sigma},L_2}\left(W_{L_2}^{s,S}\left(d_{L_2}, \boldsymbol{x}_{L_2}\right)\right) - \boldsymbol{r}_{\boldsymbol{\Sigma},L_1}\left(W_{L_1}^{u,S}\left(d_{L_1}, \boldsymbol{x}_{L_1}\right)\right) \qquad (39)
\end{aligned}
$$

where $\boldsymbol{x}_{L_1}^0$ and $\boldsymbol{x}_{L_2}^0$ are the arbitrarily selected initial states; t_{L_1} and t_{L_2} are time of orbital propagation to the objective

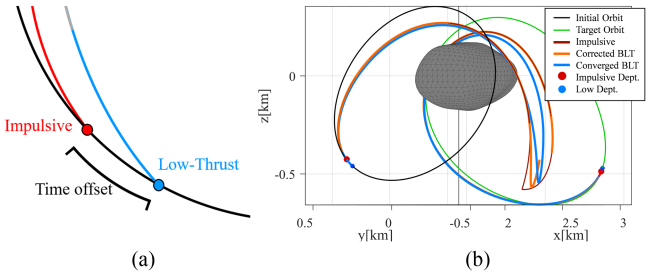

Fig. 6. Correction of control profiles. (a) Departure state is shifted backward. (b) All stages in the BLT convergence.

departure and arrival states $\boldsymbol{x}_{L_1}$ and $\boldsymbol{x}_{L_2}$; $\boldsymbol{w}_{L_1}^u$ and $\boldsymbol{w}_{L_2}^s$ are the unstable and stable eigenvector of the monodromy derived from $\boldsymbol{x}_{L_1}$ and $\boldsymbol{x}_{L_2}$; $\Delta \boldsymbol{v}_{L_1}$ and $\Delta \boldsymbol{v}_{L_2}$ are the velocity deviations in (35); $W_{L_1}^{u,S}$ and $W_{L_2}^{s,S}$ are the unstable and stable manifolds in S realm generated from $\boldsymbol{x}_{L_1}$ and $\boldsymbol{x}_{L_2}$ with deviation d_{L_1} and d_{L_2}; $\Delta \mathbf{v}_{\boldsymbol{\Sigma}}^*$ is the velocity difference of the two manifolds, $W_{L_1}^{u,S}$, $W_{L_2}^{s,S}$ at $\boldsymbol{\Sigma}$;$\Delta C_j$is the Jacobi constant gap between each manifolds; and $\Delta \mathbf{r}_{\boldsymbol{\Sigma}}$ is the position difference of the two manifolds projected on $\boldsymbol{\Sigma}$. Note that when the position constraints are satisfied in (37), so ΔC_j is equivalent to $\Delta \boldsymbol{v}_{\boldsymbol{\Sigma}}^*$ on the patching cut. What is good about ΔC_j is that on the same coasting trajectory, ΔC_j value stays consistent and can be derived directly from the departure state, while $\Delta \boldsymbol{v}_{\boldsymbol{\Sigma}}^*$ requires additional numerical trajectory integration.

In this process, especially in the S realm of the binary asteroid system, it is prone to impact with the secondary, and the area where the manifold leaves the orbit should be selected in the area far away from the secondary asteroid, referring to the classic heteroclinic connection [42, pp. 176–178]. Note that for any given two states, it is not always possible to find an optimal trajectory that satisfies the position constraints on $\boldsymbol{\Sigma}$ in the binary asteroid, that is, this problem is a constrained optimization problem. Two well-established nonlinear constrained optimizers: the sequential quadratic programming (SQP) or the interior-point method, are chosen to solve this nonlinear constrained optimal problem [40, pp. 529–546 and 563–577].

The BMPIG's conversion to BLT parameters is expressed as

$$
\boldsymbol{A}_k = \boldsymbol{B}_k = \frac{\Delta \boldsymbol{v}_k^*}{\left|\Delta \boldsymbol{v}_k^*\right|}, \quad T_k = \frac{\left|\Delta \boldsymbol{v}_k^*\right|}{a_{\text{th}}}, \quad k = L_1, L_2, \boldsymbol{\Sigma} \qquad (40)
$$

$$
t_1^{\text{coast}} = \text{TOC}\left(W_{L_1}^{u,S*}, \boldsymbol{\Sigma}\right), t_2^{\text{coast}} = \text{TOC}\left(W_{L_2}^{s,S*}, \boldsymbol{\Sigma}\right) \qquad (41)
$$

where i indicates the segments of the transfer, and $t_i^{\text{coast}}$are the time of coasting (TOC) when spacecrafts coast along the optimal manifold $W_i^{u/s,S*}$ until hitting the patching cut $\boldsymbol{\Sigma}$.

However, the time parameters derived in (37) require further correction before being applied to BMP maneuvers. Since low-thrust maneuver cannot be executed instantaneously, time offsets are needed to adjust the departure/arrival epoch and shorten the coasting segment according to the burning time (BT), as Fig. 6 shows. After that,

the corrected BLT parameters are passed to the convergence stage in Section III-D to finish the guidance.

The modified time parameters are as follows:

$$\Delta t_k = \mp T_i/2, \quad \Delta t_k^{\text{coast}} = -T_k/2 - T_{\mathbf{\Sigma}} \left(\frac{t_k^{\text{coast}*}}{t_{L_1}^{\text{coast}*} + t_{L_2}^{\text{coast}*}} \right) \quad k = L_1, L_2 \tag{42}$$

$$\begin{aligned} \boldsymbol{x}_{L_1,m} &= f\left(\Delta t_{L_1}, \boldsymbol{x}_{L_1}^*\right), \boldsymbol{x}_{L_2,m} = f\left(\Delta t_{L_2}, \boldsymbol{x}_{L_2}^*\right) \\ t_{1,m}^{\text{coast}} &= t_1^{\text{coast}} + \Delta t_1^{\text{coast}}, t_{2,m}^{\text{coast}} = t_2^{\text{coast}} + \Delta t_2^{\text{coast}} \end{aligned} \tag{43}$$

where $\boldsymbol{x}_{L_1,m}$ and $\boldsymbol{x}_{L_2,m}$ are the objective phase-modified initial and target states; and $t_{1,m}^{\text{coast}}$ and $t_{2,m}^{\text{coast}}$ are modified TOC. Similar to the case in SBIG, the modified trajectory may not converge perfectly, but it could lead to better convergence in subsequent stages.

2) UMPIG includes forward initial guess (UfMPIG), including StoS and StoO, and backward initial guess (UbMPIG), including StoS and OtoS, and only one of the initial or target orbits can generate invariant manifolds, therefore, the patching cuts should be on the stable orbits which can be possibly transcribed by the orbital elements in the case of perturbed two body orbits.

When mentioning orbital elements, the states in the synodic first need to be converted into ones in Cartesian coordinates as follows:

$$\boldsymbol{X}_{\text{in}} = \begin{bmatrix} \boldsymbol{A}_{\text{rot2in}}(t) & \boldsymbol{0} \\ \dot{\boldsymbol{A}}_{\text{rot2in}}(t) & \boldsymbol{A}_{\text{rot2in}}(t) \end{bmatrix} \boldsymbol{X}_{\text{rot}} \tag{44}$$

$$\boldsymbol{A}_{\text{rot2in}}(t) = \begin{bmatrix} \cos(T_e(t) - T_{e0}) & -\sin(T_e(t) - T_{e0}) & 0 \\ \sin(T_e(t) - T_{e0}) & \cos(T_e(t) - T_{e0}) & 0 \\ 0 & 0 & 1 \end{bmatrix} \tag{45}$$

where $\boldsymbol{X}_{\text{rot}}$ and $\boldsymbol{X}_{\text{in}}$ are states in the rotational and inertial frame, t is time duration from the initial epoch, T_{e0} is the epoch to define 66391 Moshup's initial state, and $T_e(t)$ is the current epoch. To avoid singularity, the modified equinoctial orbital elements (MEOEs) are chosen for the initial guess stages when involving orbital elements, defined as [43]

$$\begin{aligned} p_{\text{MEOE}} &= a(1 - e^2) \\ f_{\text{MEOE}} &= e\cos(\omega + \Omega) \\ g_{\text{MEOE}} &= e\sin(\omega + \Omega) \\ h_{\text{MEOE}} &= \tan(i/2)\cos(\Omega) \\ k_{\text{MEOE}} &= \tan(i/2)\sin(\Omega) \\ L_{\text{MEOE}} &= \omega + \Omega + \nu \end{aligned} \tag{46}$$

where a is the semimajor axis, e is the eccentricity, i is the inclination,ω is the argument of periapsis, Ω is the RAAN, and ν is the true anomaly of the orbit.

Recall that in UMP, one of the initial/target orbit is stable, which is designated as a planar circular orbit, for which the reasons are twofold:

1) it is hard for UMPIG to determine a patching cut on inclined or highly eccentric orbits because those orbits' topologies are ill-defined in the synodic frame;
2) the transfer design between perturbed two-body orbits has been well developed in continuous-thrust maneuver targeting (CTMT) [39].

Then, patching cut can be selected where the manifold crosses the near-circular orbits' semimajor axis (or other equivalent variables), so the position constraints are constantly satisfied, which means that ΔC_j is equivalent to $\Delta \mathbf{v}_{\mathbf{\Sigma}}$ on the patching cut like in BMPIG. Like other initial guess stages, UMPIG can achieve pseudo-OtoO based on StoS, and the impulsive UMP maneuver is derived by considering C_j gap and the realm where the manifolds intersect the initial/target orbits.

For interpretation, the optimization problem of UfMPIG is written with the denotation of transfer from L1 Lyapunov orbits to small-scale circular orbits encircling the primary asteroid where free variables are departure/arrival time and deviation in (34):t_{L_1} and d_{L_1}, and true longitude of the arrival state: L_{arr} of the circular orbits. The objective function is the sum of the two two-norm of $\Delta \mathbf{v}^*$ and C_j magnitudes

$$\begin{aligned} \boldsymbol{x}_{L_1}^* &= f\left(t_{L_1}^*, \boldsymbol{x}_{L_1}^0\right) \\ \Delta \boldsymbol{v}_{L_1}^* &= d_{L_1}^* \cdot v\left(\boldsymbol{w}_{L_1}^u\left(\boldsymbol{x}_{L_1}^*\right)\right) \\ \Delta \boldsymbol{v}_{\mathbf{\Sigma}}^* &= \boldsymbol{v}_{\mathbf{\Sigma},C_{\text{small}}}\left(L_{\text{arr}}^*\right) - \boldsymbol{v}_{\mathbf{\Sigma},L_1}\left(\mathbf{\Sigma}, W_{L_1}^{u,P}\left(d_{L_1}^*, \boldsymbol{x}_{L_1}^*\right)\right) \end{aligned} \tag{47}$$

$$\begin{aligned} \text{StoS}: L_{\text{arr}}^* &= L_{\text{arr}}, t_{L_1}^*, d_{L_1}^* \\ &= \underset{t_{L_1}, d_{L_1}}{\arg\min} \left[\Delta \boldsymbol{v}_{L_1}{}^T\left(t_{L_1}, d_{L_1}\right) \Delta \boldsymbol{v}_{L_1}\left(t_{L_1}, d_{L_1}\right) \right. \\ &\quad \left. + \left| \Delta C_j\left(L_{\text{arr}}, t_{L_1}, d_{L_1}\right) \right| \right] \end{aligned} \tag{48}$$

$$\begin{aligned} \text{StoO}: L_{\text{arr}}^*, t_{L_1}^*, d_{L_1}^* \\ = \underset{L_{\text{arr}}, t_{L_1}, d_{L_1}}{\arg\min} \left[\Delta \boldsymbol{v}_{L_1}{}^T\left(t_{L_1}, d_{L_1}\right) \Delta \boldsymbol{v}_{L_1}\left(t_{L_1}, d_{L_1}\right) \right. \\ \left. + \left| \Delta C_j\left(L_{\text{arr}}, t_{L_1}, d_{L_1}\right) \right| \right] \end{aligned} \tag{49}$$

$$\Delta C_j = C_j\left(\boldsymbol{x}_{C_{\text{small}}}\right) - C_j\left(W_{L_1}^{u,P}\left(d_{L_1}, \boldsymbol{x}_{L_1}\right)\right) \tag{50}$$

where $\boldsymbol{x}_{C_{\text{small}}}$ is the arrival state with a true longitude L_{arr} on the small-scale circular orbits, $W_{L_1}^{u,P}$ is the unstable manifold in P realm generated from $\boldsymbol{x}_{L_1}$ with deviation d_{L_1}. The remaining variables' physical interpretations are identical to the ones in (36)–(39). This unconstrained optimal problem can be solved by BFGS as well.

The conversion of UfMPIG's impulse dV to BLT low thrust is expressed according to the following equation:

$$\boldsymbol{A}_k = \boldsymbol{B}_k = \frac{\Delta \boldsymbol{v}_k^*}{\left|\Delta \boldsymbol{v}_k^*\right|}, \quad T_k = \frac{\left|\Delta \boldsymbol{v}_k^*\right|}{a_{\text{th}}} \quad \left(k = L_1, \mathbf{\Sigma}_{C_{\text{small}}}\right) \tag{51}$$

$$t_{L_1\text{toC}}^{\text{coast}} = \text{TOC}\left(W_{L_1}^{u,P*}, \mathbf{\Sigma}_{C_{\text{small}}}\left(L_{\text{arr}}^*\right)\right). \tag{52}$$

UbMPIG are interpreted with the denotation of transfer from large-scale circular orbits to L2 Lyapunov orbits, where free variables are L_{dep} and t_{L_2}, d_{L_2}, the objective function is the sum of the two two-norm of $\Delta \boldsymbol{v}^*$ and the C_j gap as well

$$\begin{aligned} \boldsymbol{x}_{L_2}^* &= f\left(t_{L_2}^*, \boldsymbol{x}_{L_2}^0\right) \\ \Delta \boldsymbol{v}_{L_2}^* &= d_{L_2}^* \cdot v\left(\boldsymbol{w}_{L_2}^s\left(\boldsymbol{x}_{L_2}^*\right)\right) \end{aligned}$$

$$\Delta \boldsymbol{v}_{\boldsymbol{\Sigma}}^{*} = \boldsymbol{v}_{\boldsymbol{\Sigma},L_2}\left(\boldsymbol{\Sigma}, W_{L_2}^{s,E}\left(d_{L_2}^{*}, \boldsymbol{x}_{L_2}^{*}\right)\right) - \boldsymbol{v}_{\boldsymbol{\Sigma},C_{\text{large}}}\left(L_{\text{dep}}^{*}\right) \quad (53)$$

$$\begin{aligned}\text{StoS}: & L_{\text{dep}}^{*} = L_{\text{dep}}, t_{L_2}^{*}, d_{L_2}^{*} \\ & = \underset{t_{L_2}, d_{L_2}}{\arg\min}\left[\Delta \boldsymbol{v}_{L_2}{}^{T}\left(t_{L_2}, d_{L_2}\right)\Delta \boldsymbol{v}_{L_2}\left(t_{L_2}, d_{L_2}\right)\right. \\ & \quad \left. + \left|\Delta C_j\left(L_{\text{dep}}, t_{L_2}, d_{L_2}\right)\right|\right] \quad (54)\end{aligned}$$

$$\begin{aligned}\text{OtoS}: & L_{\text{dep}}^{*}, t_{L_2}^{*}, d_{L_2}^{*} \\ & = \underset{L_{\text{dep}}, t_{L_2}, d_{L_2}}{\arg\min}\left[\Delta \boldsymbol{v}_{L_2}{}^{T}\left(t_{L_2}, d_{L_2}\right)\Delta \boldsymbol{v}_{L_2}\left(t_{L_2}, d_{L_2}\right)\right. \\ & \quad \left. + \left|\Delta C_j\left(L_{\text{dep}}, t_{L_2}, d_{L_2}\right)\right|\right] \quad (55)\end{aligned}$$

$$\Delta C_j = C_j\left(W_{L_2}^{s,E}\left(d_{L_2}, \boldsymbol{x}_{L_2}\right)\right) - C_j\left(\boldsymbol{x}_{C_{\text{large}}}\right) \quad (56)$$

where $\boldsymbol{x}_{C_{\text{large}}}$ is the departure state with a true longitude L_{dep} on the large-scale circular orbits, $W_{L_2}^{s,E}$ is the stable manifold in the E realm, backward generated from $\boldsymbol{x}_{L_2}$ with deviation d_{L_2}. The conversion of UbMPIG's is expressed according to the following equation:

$$\boldsymbol{A}_k = \boldsymbol{B}_k = \frac{\Delta \boldsymbol{v}_k^{*}}{\left|\Delta \boldsymbol{v}_k^{*}\right|}, \quad T_k = \frac{\left|\Delta \boldsymbol{v}_k^{*}\right|}{a_{\text{th}}}, \quad \left(k = \boldsymbol{\Sigma}_{C_{\text{large}}}, L_2\right) \quad (57)$$

$$t_{\text{CtoL}_2}^{\text{coast}} = \text{TOC}\left(W_{L_2}^{s,E*}, \boldsymbol{\Sigma}_{C_{\text{large}}}\left(L_{\text{dep}}^{*}\right)\right). \quad (58)$$

Like (42), time-related parameters in UMPIG require correction. The modifications are as follows (using subscripts in (57) and (58) namely, the UbMPIG, for interpretation purpose):

$$\begin{aligned}\Delta t_k &= \mp T_i/2 \quad \left(k = \boldsymbol{\Sigma}_{C_{\text{large}}}, L_2\right), \\ t_{\text{CtoL}_2}^{\text{coast}} &= -\left(T_{\boldsymbol{\Sigma}_{C_{\text{large}}}} + T_{L_2}\right)\Big/2 \quad (59)\\ L_{\text{dep},m} &= f\left(\Delta t_{\boldsymbol{\Sigma}_{C_{\text{large}}}}, L_{\text{dep}}^{*}\right), \boldsymbol{x}_{L_2,m} = f\left(\Delta t_{L_2}, \boldsymbol{x}_{L_2}^{*}\right) \\ t_{\text{CtoL}_2,m}^{\text{coast}} &= t_{\text{CtoL}_2}^{\text{coast}} + \Delta t_{\text{CtoL}_2}^{\text{coast}} \quad (60)\end{aligned}$$

where $L_{\text{dep},m}$ and $\boldsymbol{x}_{L_2,m}$ are the objective phase-modified initial true longitude and target states, and $t_{\text{CtoL}_2,m}^{\text{coast}}$ is modified TOC.

Time-related parameters of the UfMPIG in (51) and (52) require the same modifications before convergence stages.

D. Convergence Stage in the Realistic Dynamical Model

In the convergence stage, a realistic dynamical model (described in Section II-B2) is applied, and BCG uses NRPC [44, pp. 899–985], which is chosen for its straightforward iteration and the efficiency of updating the BLT guidance parameters $\boldsymbol{u}_0$ (i.e., $\boldsymbol{A}_0, \boldsymbol{B}_0, T_0$, etc., all initialized in Section III-C).

NRPC has two steps: first, in the "Prediction" phase, the spacecraft's states are predicted according to the initial BLT control profiles $\boldsymbol{u}_0$ and set the constraints, i.e., the error vector $\boldsymbol{e}_0$, to measure the discrepancy between the current states and the desired ones; then in the "Correction" phase, it solves the Jacobian matrix that determines the descending direction of the error $\boldsymbol{e}_i$ magnitude associated with current control profiles $\boldsymbol{u}_i$, which will be updated to be $\boldsymbol{u}_{i+1}$.

NRPC objectively approaches the error vector to null within tolerance, i.e., 1×10^{-6} by updating the guidance parameters. Then, the error $\boldsymbol{e}$ associated with control profiles $\boldsymbol{u}$ is Taylor-expanded in its neighborhood, retaining the first order

$$\boldsymbol{e}(\boldsymbol{u}^{*} + \delta \boldsymbol{u}) = \boldsymbol{e}(\boldsymbol{u}^{*}) + \partial \boldsymbol{e}/\partial \boldsymbol{u} \,.\, \delta \boldsymbol{u} + \text{O}(\delta \boldsymbol{u}^2) \quad (61)$$

where $\partial \boldsymbol{e}/\partial \boldsymbol{u}$ is the Jacobian of the error vector, this partial derivative is approximated through central finite differencing

$$\frac{\partial \boldsymbol{e}_i}{\partial \boldsymbol{u}_j} \approx \frac{\boldsymbol{e}_i(\boldsymbol{u}_0, \ldots, \boldsymbol{u}_j + \Delta \boldsymbol{u}_j, \ldots) - \boldsymbol{e}_i(\boldsymbol{u}_0, \ldots, \boldsymbol{u}_j - \Delta \boldsymbol{u}_j, \ldots)}{2\Delta \boldsymbol{u}_j}. \quad (62)$$

After putting this all together by neglecting terms of order $\delta \boldsymbol{u}^2$ or higher orders and setting (61) equal to zero, a set of linear equations of $\delta \boldsymbol{u}$ is given by

$$\boldsymbol{\Gamma} \delta \boldsymbol{u} = -\boldsymbol{e}. \quad (63)$$

Due to the difference in the number of constraints and BLT parameters, $\boldsymbol{\Gamma}$ cannot be written as a square matrix, so the pseudoinverse of $\boldsymbol{\Gamma}$ is applied to update $\mathbf{u}$ via the min-norm equation as follows:

$$\boldsymbol{u}^{j+1} = \boldsymbol{u}^{j} - \boldsymbol{\Gamma}\left(\boldsymbol{u}^{j}\right)^{T}\left[\boldsymbol{\Gamma}\left(\boldsymbol{u}^{j}\right) \,.\, \boldsymbol{\Gamma}\left(\boldsymbol{u}^{j}\right)^{T}\right]^{-1} \boldsymbol{e}\left(\boldsymbol{u}^{j}\right). \quad (64)$$

Due to the highly nonlinear dynamical environment, the results of each iteration are not always in the descending directions, so a line search is necessary, where the step length factor is set to 1/10. One fact that needs to be noticed is that when current $\boldsymbol{u}$ guides a trajectory impacting the asteroids (this is very common in the binary asteroid systems), the algorithm will perform another internal line search; the step length factor is set to 0.5 until it breaks away from the impact. An upper limit of iterations is needed to prevent wasting too much time on an invalid $\boldsymbol{u}$.

This process is repeatedly executed until the two-norm of the constraint vector $\boldsymbol{e}$ converges within a tolerance of 1×10^{-6} corresponding to a position error of 2.55 mm, and a speed error of 0.25μm/s.

The construction of NRPC's $\boldsymbol{u}$. and $\boldsymbol{e}$ in different scenarios will be detailed in the following part of this section. Notably, the StoS types used in the convergence have nothing to do with the initial guess types though they share the same names. They can be combined arbitrarily, that is, initial guess can use OtoS, while converging with StoS, etc. Any transfer involving a two-body-like orbit can use the type containing "O"; and StoS is studied in this section for it is the transfer with the highest convergence difficulty and the most compatible control for special orbits in CR3BP owing to the aforementioned reasons in Section III-C1. So can BCG's StoS be applied to transfers in total perturbed two-body problems (i.e., none of Lyapunov or Halo orbits involved), and its iteration form can be degenerated to any kind of O/StoO/S transfer.

1) *Single Burn:* Consider a formation that is composed of two spacecraft in elliptical Keplerian orbits

$$\text{S2S}: \boldsymbol{u} = \begin{bmatrix}\boldsymbol{A} \\ \boldsymbol{B} \\ T\end{bmatrix}_{7\times 1}, \quad \boldsymbol{e} = \left[\boldsymbol{x}(t_f) - \boldsymbol{x}_f\right]_{6\times 1}$$

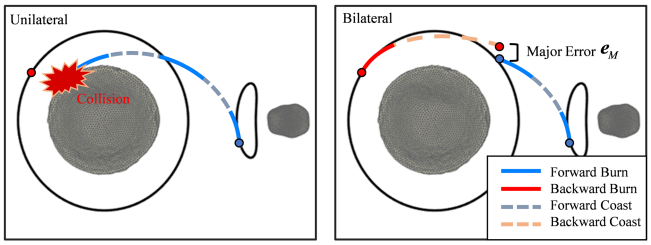

Fig. 7. Comparison between (a) unilateral and (b) bilateral propagations.

$$t_f = t_0 + T \tag{65}$$

$$\boldsymbol{\Gamma} = \frac{\partial \boldsymbol{e}}{\partial \boldsymbol{u}} \tag{66}$$

where t_f and t_0 are the initial and terminal time, $\boldsymbol{x}(t_f)$ is the terminal state, and $\boldsymbol{x}_f$ is the target state. The error is calculated unilaterally (i.e., only one time of trajectory integration from the initial to the terminal in each iteration).

2) *Multiple-Burn Leveraging Manifolds:* Due to the severe dynamical drift in CR3BP and nonlinearity in longer trajectories, the unilateral error propagation introduced in single-burn convergence is prone to collide with central bodies when is applied to multiple burns, as shown in Fig. 7(a), in which cases these outliers interfere with the descending directions of errors or even loop the algorithm infinitely.

A bilateral propagation is purposed in multiple burn's convergence, which segregates the trajectory into the forward and backward segments, as shown in Fig. 7(b); the major error $\mathbf{e}_M$ is the 6-D state error on the virtual point where the initial backward and forward trajectories meet. Actually, each side's trajectory is propagated according to the initial parameters, and the ends of both sides do not meet at all, causing this relatively large gap.

This refined method reduces the probability of collision and the difficulty in convergence during the propagation. Then, a smaller two-norm of the error vector $\mathbf{e}$ at the first iteration epoch is obtained thanks to the shorter numerical integration from the two ends. All of this leads to a faster convergence.

In the multiple-burn convergence, the iterative matrix is changed to the form of patched matrices

$$\boldsymbol{\Gamma}\delta \boldsymbol{U} = -\boldsymbol{E} \tag{67}$$

where

$$\boldsymbol{U} = \begin{bmatrix} \boldsymbol{u}_1 & \cdots & \boldsymbol{u}_n \end{bmatrix}^T, \quad \boldsymbol{E} = \begin{bmatrix} \boldsymbol{e}_1 & \cdots & \boldsymbol{e}_n \end{bmatrix}^T. \tag{68}$$

1) In the convergence stage of BMP, taking a five-segment maneuver of burn–coast–burn–coast–burn in Fig. 7 as an example, Fig. 8 shows its prediction stage. The trajectory is demonstrated horizontally for interpretation purposes where the legends share the same meaning with Fig. 7. The superscript b and the dark red paths represent the flow of the backward prediction, and the dark blue paths and variables without superscripts represent the forward prediction.

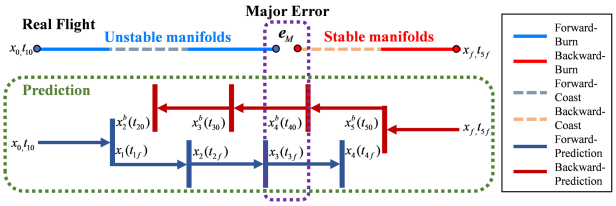

Fig. 8. Prediction phase of BMP.

The error is calculated at each interface, and the third one is chosen to be the major error $\boldsymbol{e}_M$ for the real flight trajectory intersects in this specific case. However, it can be shifted to any of the interface among 12,3, and 4, if necessary. Then, the control profiles are defined as follows:

$$\text{StoS}: \boldsymbol{u}_1 = \begin{bmatrix} \boldsymbol{A}_1 \\ \boldsymbol{B}_1 \\ T_1 \end{bmatrix}_{7\times 1}, \boldsymbol{u}_2 = \begin{bmatrix} \boldsymbol{x}_2^b(t_{20}) \\ t_{2,m}^{\text{coast}} \end{bmatrix}_{7\times 1} \quad \boldsymbol{u}_3 = \begin{bmatrix} \boldsymbol{x}_3^b(t_{30}) \\ \boldsymbol{A}_3 \\ \boldsymbol{B}_3 \\ T_3 \end{bmatrix}_{13\times 1}$$

$$\boldsymbol{u}_4 = \begin{bmatrix} \boldsymbol{x}_4(t_{4f}) \\ t_{4,m}^{\text{coast}} \end{bmatrix}_{7\times 1}, \quad \boldsymbol{u}_5 = \begin{bmatrix} \boldsymbol{A}_5 \\ \boldsymbol{B}_5 \\ T_5 \end{bmatrix}_{7\times 1} \tag{69}$$

$$\boldsymbol{e}_i = \left[\boldsymbol{x}_i(t_{i,f}) - \boldsymbol{x}_{i+1}^b(t_{i+1,0})\right]_{6\times 1} \quad i = 1, 2, 3, 4, 5 \tag{70}$$

where

$$\begin{aligned} t_{1f} &= t_{10} + T_1 & t_{10} &= t_i \\ t_{2f} &= t_{1f} + t_{2,m}^{\text{coast}} & t_{20} &= t_{30} - t_{2m}^{\text{coast}} \\ t_{3f} &= t_{2f} + T_3 & t_{30} &= t_{40} - T_3 \\ t_{4f} &= t_{3f} + t_{4,m}^{\text{coast}} & t_{40} &= t_{50} - t_{4m}^{\text{coast}} \\ t_{5f} &= t_f & t_{50} &= t_{5f} - T_4 \end{aligned} \tag{71}$$

where subscript 0 and f indicate the initial and final state of each segment, the subscript 1 indicates variables in the first burning segment, the subscript 2 is for the first coasting segment, the subscript 3 is for the second burning segment, the subscript 4 is for the second coasting segment, and the subscript 5 is for the final burning segment. Note that $\boldsymbol{u}_i (i = 2, 3, 4)$ include state variables that are initialized by a single run of the prediction stage with initial $\boldsymbol{u}_0$ directly derived in (40)–(43)

$$\begin{aligned} \boldsymbol{x}_{\boldsymbol{u}_2}^0 &= \left(\boldsymbol{x}_2^{b0}(t_{20}) + \boldsymbol{x}_1^0(t_{1f})\right)/2 \\ \boldsymbol{x}_{\boldsymbol{u}_3}^0 &= \left(\boldsymbol{x}_3^{b0}(t_{30}) + \boldsymbol{x}_2^0(t_{2f})\right)/2 \\ \boldsymbol{x}_{\boldsymbol{u}_4}^0 &= \left(\boldsymbol{x}_5^{b0}(t_{50}) + \boldsymbol{x}_4^0(t_{4f})\right)/2. \end{aligned} \tag{72}$$

The Jacobian matrix $\boldsymbol{\Gamma}$ becomes

$$\boldsymbol{\Gamma} = \frac{\partial \boldsymbol{E}}{\partial \boldsymbol{U}} = \begin{bmatrix} \frac{\partial \boldsymbol{e}_1}{\partial \boldsymbol{u}_1}_{(6\times 7)} & -I_{(6\times 7)} & & \\ & \frac{\partial \boldsymbol{e}_2}{\partial \boldsymbol{u}_2}_{(6\times 7)} & -I_{(6\times 13)} & \\ & & \frac{\partial \boldsymbol{e}_3}{\partial \boldsymbol{u}_3}_{(6\times 13)} & -\frac{\partial \boldsymbol{e}_3}{\partial \boldsymbol{u}_4}_{(6\times 7)} \\ & & & I_{(6\times 7)} \quad -\frac{\partial \boldsymbol{e}_4}{\partial \boldsymbol{u}_5}_{(6\times 7)} \end{bmatrix} \tag{73}$$

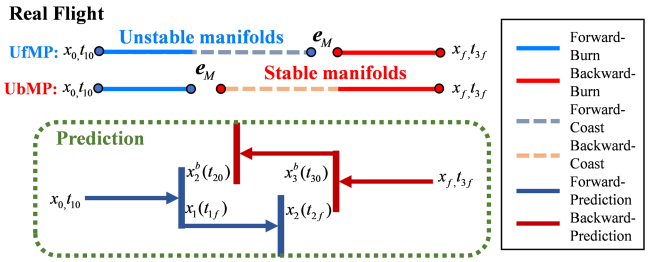

Fig. 9. Prediction phase of unilateral forward and backward manifold patching.

where $\frac{\partial \boldsymbol{e}_i}{\partial \boldsymbol{u}_i}$s are derived by central finite differencing, and $I_{(6\times7)}$ and $I_{(6\times13)}$ are identity matrices with zeros to fill up the rest of the columns.

2) The prediction flow of UMP is shown in Fig. 9. The control profiles and error vectors in the form of StoS are defined as

UfMP_StoS :

$$\boldsymbol{u}_1 = \begin{bmatrix} \boldsymbol{A}_1 \\ \boldsymbol{B}_1 \\ T_1 \end{bmatrix}_{7\times1}, \quad \boldsymbol{u}_2 = \begin{bmatrix} \boldsymbol{x}_2^b(t_{20}) \\ t_{2,m}^{\text{coast}} \end{bmatrix}_{7\times1} \quad \boldsymbol{u}_3 = \begin{bmatrix} \boldsymbol{A}_3 \\ \boldsymbol{B}_3 \\ T_3 \end{bmatrix}_{13\times1} \tag{74}$$

UbMP_StoS :

$$\boldsymbol{u}_1 = \begin{bmatrix} \boldsymbol{A}_1 \\ \boldsymbol{B}_1 \\ T_1 \end{bmatrix}_{7\times1}, \quad \boldsymbol{u}_2 = \begin{bmatrix} \boldsymbol{x}_2(t_{2f}) \\ t_{2,m}^{\text{coast}} \end{bmatrix}_{7\times1} \quad \boldsymbol{u}_3 = \begin{bmatrix} \boldsymbol{A}_3 \\ \boldsymbol{B}_3 \\ T_3 \end{bmatrix}_{13\times1} \tag{75}$$

$$\boldsymbol{e}_i = \left[\boldsymbol{x}_i(t_{i,f}) - \boldsymbol{x}_{i+1}^b(t_{i+1,0})\right]_{6\times1} \quad i = 1, 2. \tag{76}$$

The Jacobian matrix $\boldsymbol{\Gamma}$ becomes

$$\text{UfMP\_StoS} : \boldsymbol{\Gamma} = \frac{\partial \boldsymbol{E}}{\partial \boldsymbol{U}} = \begin{bmatrix} \frac{\partial \boldsymbol{e}_1}{\partial \boldsymbol{u}_1}_{(6\times7)} & -I_{(6\times7)} & \\ & \frac{\partial \boldsymbol{e}_2}{\partial \boldsymbol{u}_2}_{(6\times7)} & \frac{\partial \boldsymbol{e}_3}{\partial \boldsymbol{u}_3}_{(6\times7)} \end{bmatrix} \tag{77}$$

$$\text{UbMP\_StoS} : \boldsymbol{\Gamma} = \frac{\partial \boldsymbol{E}}{\partial \boldsymbol{U}} = \begin{bmatrix} \frac{\partial \boldsymbol{e}_1}{\partial \boldsymbol{u}_1}_{(6\times7)} & -\frac{\partial \boldsymbol{e}_2}{\partial \boldsymbol{u}_2}_{(6\times7)} & \\ & I_{(6\times7)} & \frac{\partial \boldsymbol{e}_2}{\partial \boldsymbol{u}_3}_{(6\times7)} \end{bmatrix} \tag{78}$$

where $\frac{\partial \boldsymbol{e}_i}{\partial \boldsymbol{u}_i}$s are derived by central finite differencing, and $I_{(6\times7)}$ are identity matrices with zeros to fill up for the rest of the columns.

IV. CONSTANT-THRUST TRANSFERS ABOUT A BINARY ASTEROID SYSTEM

In this section, the versatile StoS single-burn and multiple-burn BLT maneuvers devised by BCG were performed about 66391 Moshup, using a 600-kg spacecraft with a solar projected area A_{sc} of 12.5 m × 4 m and equivalent reflectivity to solar radiation C_R of 1.5 (all similar to the DART spacecraft [2]) using a low-thrust engine with varying constant-thrust levels. The influence on power supply caused by the shadow area of the asteroid is neglected. The same spacecraft and assumption will be applied to Section V.

TABLE II
Performance of Finite Thruster

Thrusters	Input Power[kW]	F[mN]	I_{sp} [s]
BHT-600[45]	1.5	90	1660
NSTAR[46]	2.3	92	1700
NEXT[47]	6.9	236	4190
BHT-8000[48]	8	449	2210

The trajectories demonstrated in this section are chosen for possible task demands for remote sensing, sampling, or other applications. It mainly includes approaching and circumscribing orbits (from the large-scale orbits, entering the S realm at the L2 point, from L1 to the P realm, and approaching the small-scale orbits near the primary). Due to the reversibility of StoS, the backward process has exactly the same difficulty and process as the forward process.

A. Single Burn

Four StoS single-burn constant low-thrust orbital transfers using various thrust levels mapped out by BCG were simulated in this section.

The orbital transfers consist of the following:

1) a long coplanar transfer between L2 and L1 Lyapunov orbits with C_j gap;
2) a noncoplanar transfer between L2 and L1 southern Halo orbits;
3) a close noncoplanar transfer maneuver from L1 Halo to L1 Lyapunov orbit;
4) a long noncoplanar maneuver from L1 Lyapunov orbit to L5 vertical Lyapunov orbit.

The results are shown in Fig. 10.

For reference, a 15-mN (corresponding acceleration is 2.5×10^{-5}m/s^2) thruster with a specific impulse of 2000 s can perform transfer from L1 to L5 [see Fig. 10(d)] in 5.88 h and with fuel usage of only 16.28 g.

Table II shows the test data of low-thrust ion thrusters that have been or will be used in deep space missions. The NEXT, already equipped for DART mission, provides a maximum thrust of 236 mN corresponding to 3.9×10^{-4}m/s^2 and it is 1.3×10^{-4}m/s^2 for NSTAR equipped for DeepSpace-1 and DAWN mission, both far exceeding the minimum executable acceleration for transfers in Fig. 10. The C_j and control histories of maneuver in Fig. 10(b) with different thrust levels are shown in Fig. 11(a) and (b). As Fig. 11(a) shows, the transfer orbits associated with all levels of thrust levels go far beyond the C_j gap between ones of the two ends along the trajectory. This very "prodigal" and fuel-inefficient maneuver, however, speaks to the high control authority of low-thrust BLT maneuvers about 66391 Moshup as it allows spacecraft to complete transfer despite the poor initial condition.

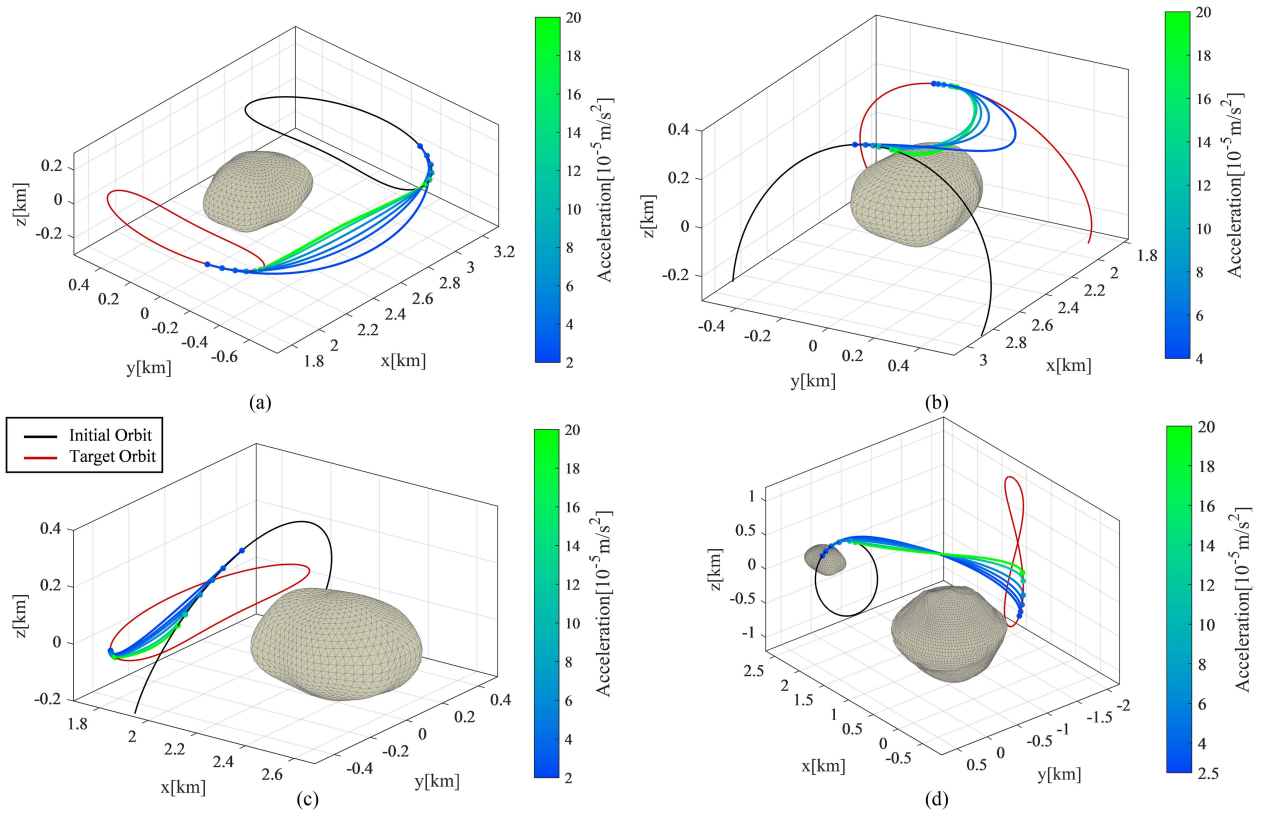

Fig. 10. Single-burn StoS transfers. (a) Coplanar transfer between Lyapunov orbits. (b) Noncoplanar transfer between Halo orbits. (c) Noncoplanar transfer between Halo and Lyapunov orbits. (d) Noncoplanar transfer between colinear and triangular libration orbits.

B. Multiple-Burn Leveraging Manifolds

Four StoS multiple-burn orbital transfers using various thrust levels mapped out by BCG were simulated in this section.

The reverse initial and target orbits in Fig. 10(a) and (b) were chosen for BMP maneuver as follows:

1) a transfer from L1 Lyapunov to L2 Lyapunov;
2) a transfer from L1 Halo to L2 Halo.

And for UMP maneuver, it is chosen as follows:

1) a transfer to enter the P realm to a small-scale orbit encircling the primary via the L1 point initialized by OtoS unilateral backward initial guess;
2) a transfer from a large-scale orbit to enter the S realm via the L2 point initialized by StoO unilateral forward initial guess.

The results are shown in Fig. 12, where dark red dots denote the impulsive maneuvers initialized by initial guess stages.

The C_j and control histories of maneuver in Fig. 12(b) with different thrust levels are shown in Fig. 11(c) and (d). The colored lines represent the thrusting section and the gray lines are for the coasting section in Figs. 11, 13, and 14.

For comparison purposes, a reversed multiple-burn transfer (L1 to L2 Halo orbits) with the same C_j gap as the single burn in Fig. 10(b) (L2 to L1 Halo orbits) is shown in Fig. 12(b). Compared with single burn, multiple burns are much more dependent on the dynamic characteristics of CR3BP. The flight time is less relevant with thrust levels in multiple-burn transfer, usually tens of times more than that of single burn transfer, while fuel usage is almost exponentially reduced. For reference, when using a 24-mN thruster (i.e., $4 \times 10^{-5}\text{m/s}^2$) with a specific impulse of 2000 s in both scenarios, the time of flight and fuel usage are 190 min/814 min and 13.64 g/3.38 g for single/multiple burns. The minimum executable acceleration is examined to be smaller than that of single burn as well.

An insight into the C_j and control history is shown in Fig. 11(c) and (d). The excessive part beyond C_j gap (outlined by red dash) is rather marginal than in Fig. 11(a), speaking to multiple burn's fuel efficiency from an energy aspect.

V. PERFORMANCE ANALYSIS

In this section, different aspects of the BCG's performance will be examined using some numerical methods. First, the robustness is validated in the same scenario by an assortment of initial perturbation levels, each with an $N = 600$ Monte Carlo convergence simulation across a wide array of thrust levels. Then, BCG is compared with true optimal methods derived by interior point (IP) optimization to demonstrate the balance between optimality and efficiency of this guidance method.

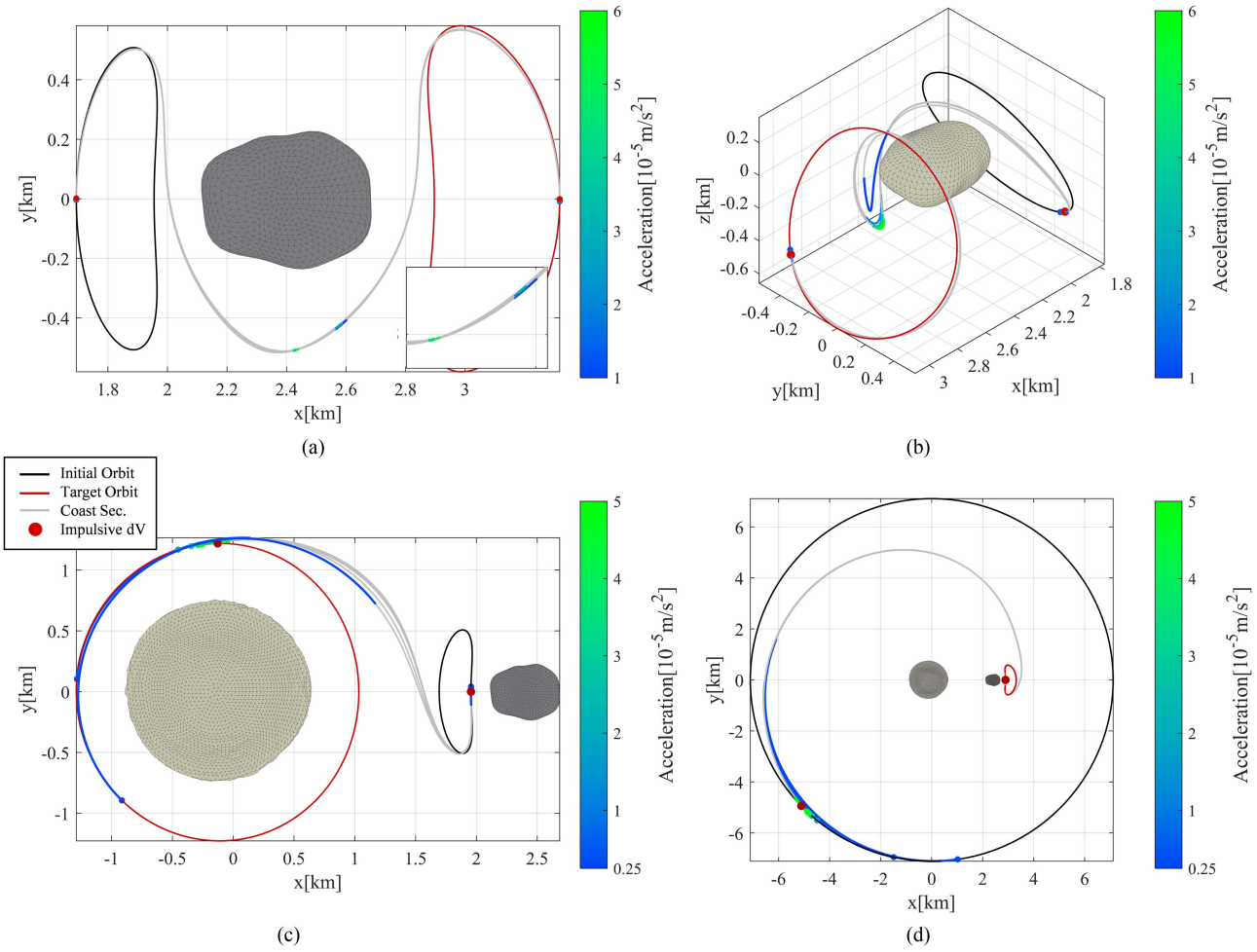

Fig. 11. (a) and (b) $C_j$histories of maneuvers in Figs. 10(b) and 12(b). (c) and (d) Control histories of maneuvers in Figs. 10(b) and 12(b) with different thrust levels.

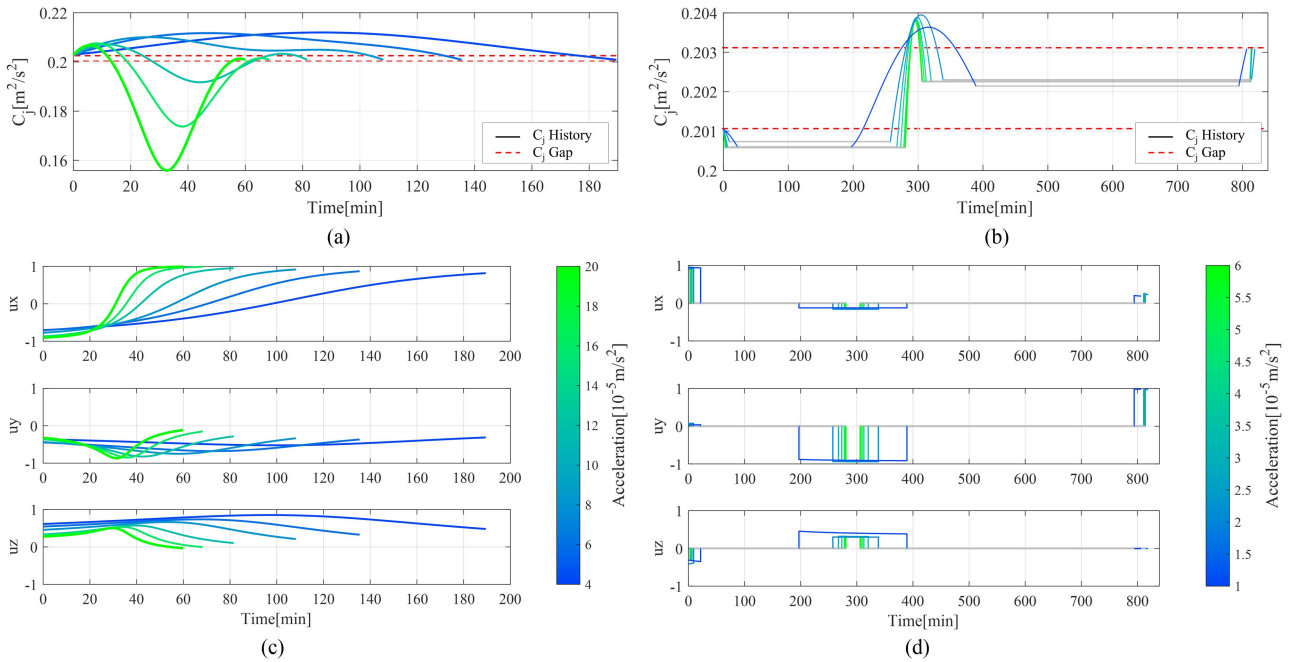

Fig. 12. Multiple-burn StoS transfers. (a) Coplanar transfer between Lyapunov orbits. (b) Noncoplanar transfer between Halo orbits. (c) Transfer from L1 to small-scale orbit in P realm. (d) Transfer from large-scale orbit in the exterior realm to L2.

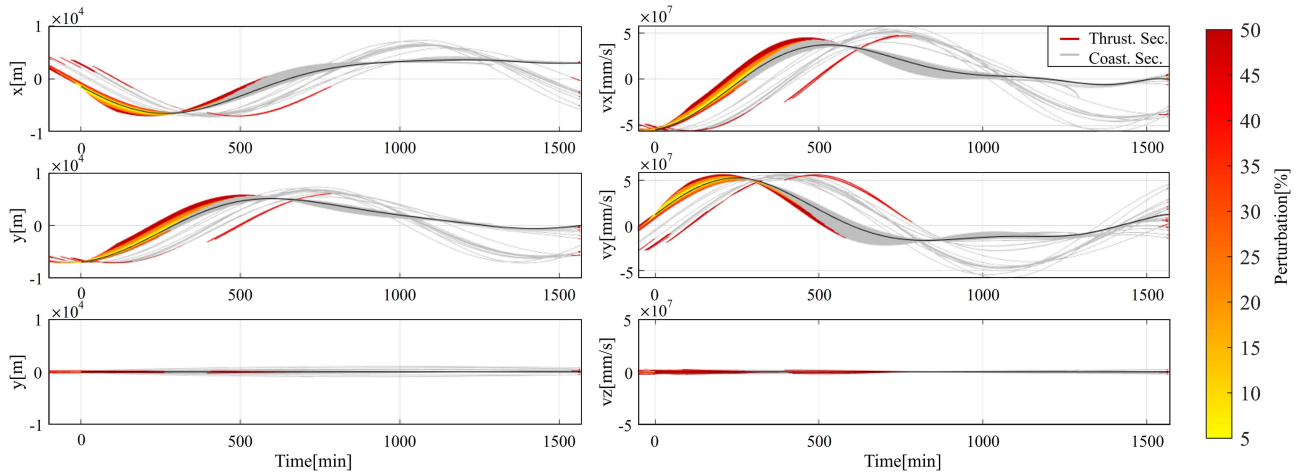

Fig. 13. Perturbed states of several $N = 600$ backward-propagated initial perturbation simulations with 2.4 mN.

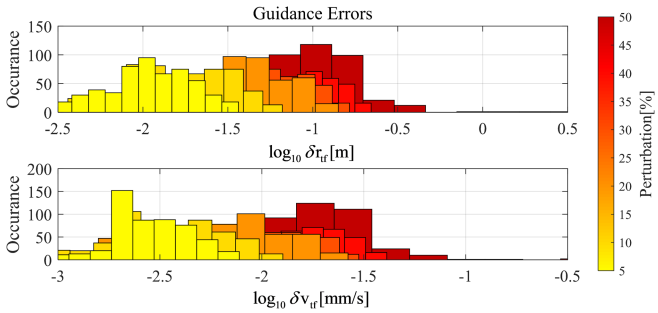

Fig. 14. Histogram of the position and velocity errors of several $N = 600$ with 2.4 mN.

A. Robustness Validation of BLT in CR3BP

In the robustness validation, the nominal maneuver is chosen as an UMP StoS maneuver from a random position on a circular, 3-km planar orbit to fixed positions on target L2 Lyapunov orbits shown in Fig. 12(d), chosen for providing a fuel-efficient and safe way to approach an asteroid when the spacecraft transfers from the heliocentric orbits to proximity orbits.

StoS, the most basic convergence type in BLT, is the most difficult to converge due to its least free variable to constraint ratio. So, it can be used to give a strict convergence tolerance under perturbations, yielding a quantitative analysis of BCG's capability of converging on low-thrust transfers.

Furthermore, UMP, essentially a burn-coast-burn maneuver, is chosen because it is the most versatile maneuver type the BCG can design. When the interval coasting segment decreases to null, UMP multiple burns degenerate into single-burn maneuvers. The architecture of coast–burn can be extended to construct longer trajectories with more segments.

In this section, the performance of the transfer maneuver convergence is tested with $N = 600$ initial state perturbations (e.g., ignition delay, positioning error, or discrepant gravitational field, which causes the deviation of the maneuver starting position from the expected position). A maximum iteration of 40 and a convergence tolerance of 5×10^{-5} are imposed on robustness validation.

This process was performed with the constant-thrust maneuver shown in Fig. 12(d), where the BLT guidance parameters and departure state were perturbed by values up to 5, 10, 20, 30, 40, and 50% from the nominal trajectory and aimed at the same target orbit. The orbit determination for the initial and target orbits is assumed to be accurate.

Figs. 13 and 14 illustrate the results of 2.4-mN thrust (i.e., 4×10^{-6}m/s^2).

For visualization, Fig. 13(a) shows the $N = 600$ position and velocity components along the trajectory in the synodic frame, where the black curve represents the nominal trajectory. In Fig. 13(a), the time offset of each trajectory is adjusted to end for the same epoch, so the unconverged maneuvers that ended up with less time of flight (e.g., colliding with the asteroid, or failing to converge within set iteration limit) will be salient and outlying. Fig. 14 shows the histogram of the two-norm of the position and velocity errors. Since the initial state perturbation is applied according to the normal distribution, the error remains approximately Gaussian when the initial perturbation level is small. As the initial perturbation increases, the errors become less Gaussian, and are concentrated in the region of larger errors.

Fig. 15 shows the convergence histogram with higher thrust levels (30 mN, 5×10^{-5}m/s^2). It is obvious that the convergence rate and accuracy increase significantly with larger thrust, and the results in the histogram maintain Gaussian even with greater initial perturbation.

Table III shows the results of the convergence validation. Since the convergence of the Newton method is limited within sufficiently good initial guesses, an interesting result is that the Monte Carlo simulation quantifies the range of the initial error, beyond which BCG begins to crash down. With a 30-mN thruster, BCG achieves over 98% convergence at 10% perturbation, and over 80% convergence at 20% perturbation. When it is perturbed beyond 20%, the convergence rate exhibits a steep descent.

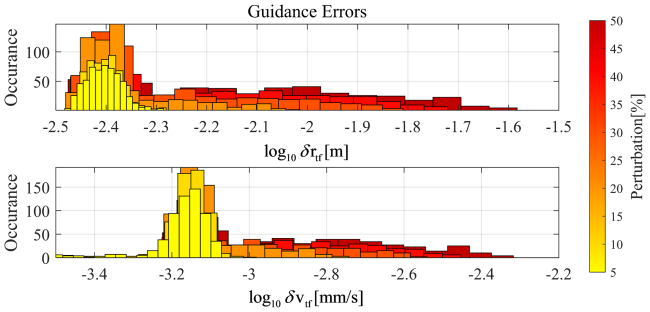

Fig. 15. Histogram of the position and velocity errors of several $N = 600$ with 30 mN.

TABLE III
Perturbated Trajectory Statistics With 2.4 and 30 mN

Perturbation [%]	2.4mN Converged [%]	30mNConverged [%]
5	94.66	99.15
10	79.83	98.47
20	50.00	80.51
30	33.27	59.64
40	26.03	47.86
50	19.13	40.00

B. Computational Efficiency and Comparison to Optimal Results

The previous Monte Carlo simulations show that the BCG is capable of overcoming initial state perturbations. The computational and fuel efficiency of the maneuver are equivalently important. This section compares the BCG low-thrust BLT maneuver calculated in Fig. 12 with the optimized constant low-thrust maneuver calculated by the IP optimization via SCIPY.

To measure BCG's optimality, the objective function of IP is set to be BT optimal. The IP method uses the same initial control profiles derived by MBIG in Section III-C1. Fig. 17 compares the maneuver calculated by BCG and the optimal maneuver calculated by the IP. Fig. 17(a) shows the iteration time of IP divided by that of BCG. Fig. 17(b) shows the BT of the IP optimal maneuver divided by the BT of the BCG. Fig. 16 examines the control vectors and C_j for BCG and IP optimal transfer between L1 and L2 Halo orbits in Fig. 12(b).

As shown in Fig. 17(a), the efficiency of the BCG algorithm is much higher than that of the IP optimization, especially when the thrust acceleration is low. As the thrust increases, the efficiency gap of a given transfer decreases gradually, especially for the higher thrust level, which almost resembles the impulsive initial guess. For longer transfers in Fig. 12(a) and (b), implementing BMP, due to the multitude of segments and the complexity of the Jacobian matrix, the computational efficiency promotion of BCG is not eminent, only several times faster than IP. For the maneuver of Fig. 12(a), at the maximum tested thrust of 240 mN ($4 \times 10^{-4}\text{m/s}^2$), the computational costs are almost identical. For transfers in Fig. 12(c) and (d), using UMP with fewer segments, the relative efficiency of the BCG is very considerable. Especially for the shortest transfer in Fig. 12(d), even when the thrust is 1.5 mN ($2.5 \times 10^{-6}\text{m/s}^2$), BCG took only 11 iterations or 14 s to converge within the tolerance of 1×10^{-6}.

In Fig. 17(b), the BT of the IP's true optimal maneuver is marginally better than that of BCG, especially when the spacecraft performs some aggressive noncoplanar maneuvers about asteroids. Taking control profiles in Fig. 12(b) (shown in Fig. 16), the optimal IP result has a milder amplitude in the control direction and less surplus C_j along the trajectory. For Fig. 12(b), the fuel reduction can be achieved by 9% when using 1.5 mN ($2.5 \times 10^{-6}\text{m/s}^2$), saving up to 46 min of BT, corresponding to 1.3124 g of fuel, however, it takes almost 200 times longer to calculate. Furthermore, these simulations were performed on a 2.6-GHz Intel Core i7-10750H processor. As the BCG algorithm was written in PYTHON 3.9, the speed of BCG can be further improved by coding in a mixed compiled language (with C++ or MEX).

VI. DISCUSSION

The results of Section V show that the BCG algorithm is an efficient and robust constant low-thrust guidance algorithm with an appropriate thrust level in the case of 66391 Moshup.

However, according to the $N = 600$ Monte Carlo, convergence limits do exist. For instance, when the thrust is 30 mN, the convergence rate drops sharply when the initial perturbation exceeds 20%. This may be due to the BCG's simple derivation, which transforms some nonlinear problems into linear problems (e.g., direct conversion from impulsive to BLT initial guesses about binary asteroids by neglecting the uniform gravitational assumption for BLT [38], using finite segments of a low-thrust trajectory, etc.).

Although the simplicity of BCG allows for efficiency, it also restricts BCG's capability to design more complex and longer transfers. The manifold patching used in the initial guess stage is based on the heteroclinic connection manifolds less than one revolution. For instance, there is a probability of finding better (e.g., with less $\Delta\mathbf{v}$) patching cuts by applying multirevolutionary heteroclinic connections between L1 and L2 as an initial guess [42]. Considering that the BLT is based on the uniform gravitational assumption, a longer orbit will add nonlinearity to the algorithm. This can be achieved by increasing the number of segments in the convergence stage. Still, more segments also account for computational inefficiency since the Jacobian matrix of Newton's method becomes far more complex.

The results in Section V-B show BCG's tradeoff on computational efficiency and optimality. BCG tends to be more efficient when handling trajectories with lower thrust levels and fewer segments. Conversely, near optimality worsens as the thrust gets smaller, compared to the true optimum.

Finally, it took more iterations to solve the impulsive initial guess in the initial guess stage than in the convergence phase (for BFGS, SQP, and interior-point methods in Section III-C, the maximum iteration is 80, for NRPC in Section III-D, it is 40), which seems counterintuitive since

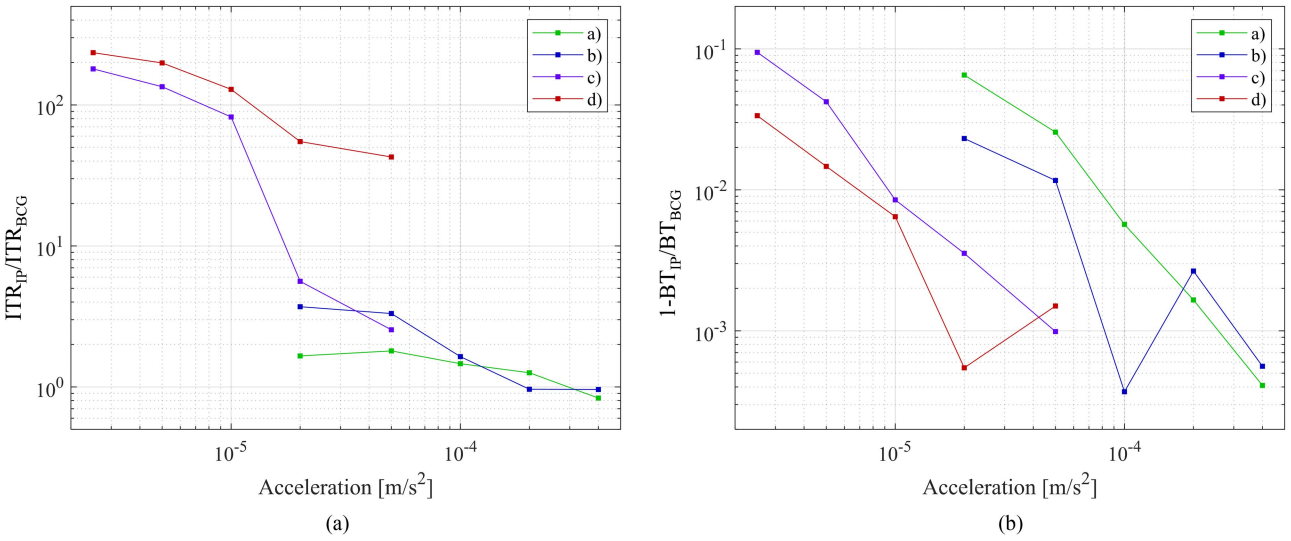

Fig. 16. Comparison between BCG and IP optimization for maneuvers shown in Fig. 12(b). (a) C_j and (b) Control history.

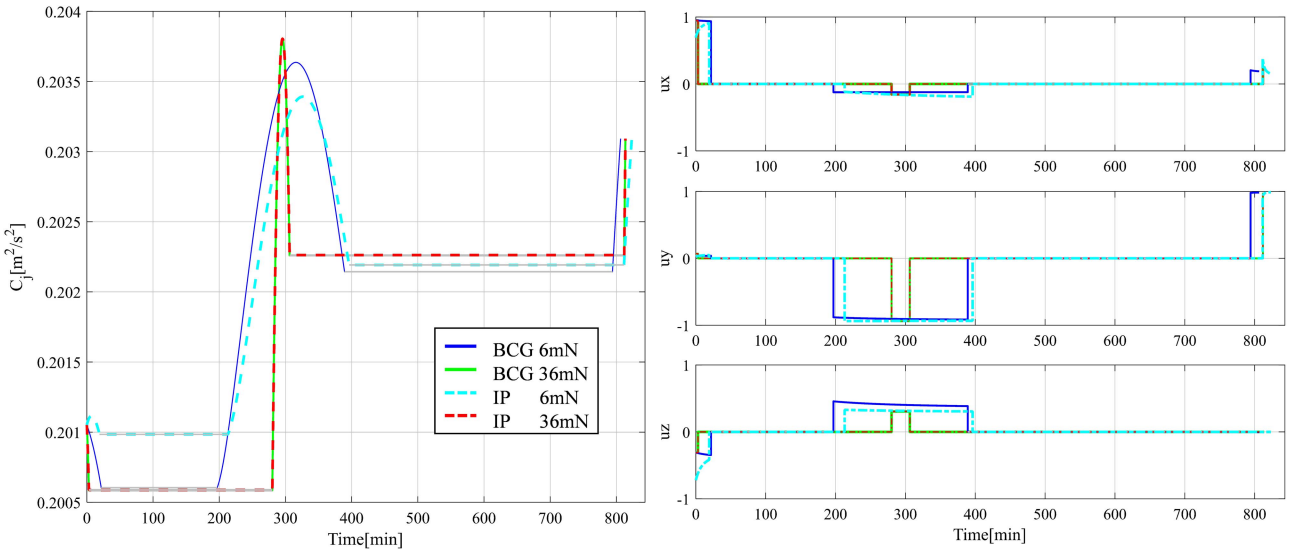

Fig. 17. Comparison between BCG and IP optimization for maneuvers shown in Fig. 12. (a) Iteration time. (b) Burning time (BT).

the convergence is more stringent due to the trajectory continuity. It is caused by the fact that orbital motion associated with equilibriums in CR3BP in the synodic frame cannot be expressed in closed forms, thus making it difficult to be exported into the six-variable orbital elements. BCG uses an alternative pseudo-OtoO by orbital propagation on the target and initial orbits to release the phase constraints in the initial guess stage. This methodology introduces more variables instead, while a true OtoO based on orbital elements reduces variables. It is imperative to notice that pseudo-OtoO does reduce the absolute difficulty of convergence on an initial guess, however.

If the orbital motion near the binary asteroids can be derived in closed forms, and then, parameterized as in a point-mass CR3BP [49], the initial guess stage of BCG will be more efficient, and there will be a plethora of options in the convergence stage.

VII. CONCLUSION

This article introduces a fuel-efficient BCG algorithm capable of planning low-thrust transfers about a binary asteroid system. The BCG algorithm uses a BLT guidance law, manifold patching techniques, and Newton–Raphson predictor–corrector to design a variety of executable single-burn and multiple-burn transfer trajectories. This work has applied BCG to a plethora of transfer scenarios in the study case of 66391 Moshup and shown BCG-guided low-thrust maneuvers' high fuel efficiency when performing aggressive noncoplanar transfers between orbits in the binary asteroid system for only grams of fuel. And through a multitude of Monte Carlo simulations, this work has demonstrated BCG's robustness against strong initial state perturbation. Finally, BCG's tradeoff between computational efficiency and near-optimality has been proven excellent by comparison with well-established optimization methods. At

a high level, the BCG algorithm converts trajectory design into linear optimization problems, which allows for high computational efficiency, maintaining near optimality in the meantime. For example, with a 1.5-mN thruster (i.e., $2.5 \times 10^{-6}\mathrm{m/s^2}$), BCG can converge over 200 times faster than IP optimization while costs only 9% more than the true optimal trajectory in fuel. Furthermore, if the close form parameters, like orbital elements of the orbital motion near the binary asteroids, can be obtained, the versatility and computational efficiency of BCG will be further enhanced. In conclusion, BCG, in terms of fuel and computation efficiency, will be a promising option for low-thrust spacecraft's autonomous guidance about binary asteroids.

REFERENCE

[1] B. N. Sharkey, V. Reddy, J. A. Sanchez, M. R. Izawa, and J. P. Emery, "Compositional constraints for Lucy mission Trojan asteroids via near-infrared spectroscopy," *Astronomical J.*, vol. 158, no. 5, pp. 204–216, 2019.

[2] A. Cheng, P. Michel, C. Reed, A. Galvez, I. Carnelli, and P. Headquarters, "Dart: Double asteroid redirection test," in *Proc. Eur. Planet. Sci. Congr.*, 2012, pp. 23–28.

[3] P. Michel et al., "European component of the AIDA mission to a binary asteroid: Characterization and interpretation of the impact of the DART mission," *Adv. Space Res.*, vol. 62, no. 8, pp. 2261–2272, 2018.

[4] *Nammo-Westcottliquid-engine-LEROS1C*, Nov. 26, 2023. [Online]. Available: https://www.nammo.com/wp-content/uploads/2021/03/2021-Nammo-Westcott-Liquid-Engine-LEROS1C.pdf

[5] K. Berry et al., "OSIRIS-REX touch-and-go (TAG) mission design and analysis," in *Proc. 36th Annu. AAS Guid. Control Conf.*, 2013.

[6] L. Kumar and S. Jain, "Electric propulsion system for electric vehicular technology: A review," *Renewable Sustain. Energy Rev.*, vol. 29, pp. 924–940, 2014.

[7] M. D. Rayman, P. A. Chadbourne, J. S. Culwell, and S. N. Williams, "Mission design for deep space 1: A low-thrust technology validation mission," *Acta Astronautica*, vol. 45, no. 4–9, pp. 381–388, 1999.

[8] Y. Tsuda, M. Yoshikawa, M. Abe, H. Minamino, and S. Nakazawa, "System design of the Hayabusa 2—Asteroid sample return mission to 1999 JU3," *Acta Astronautica*, vol. 91, pp. 356–362, 2013.

[9] G. Ono et al., "Design and flight results of GNC systems in Hayabusa2 descent operations," *Astrodynamics*, vol. 4, pp. 105–117, 2020.

[10] D. Morante, M. S. Rivo, and M. Soler, "A survey on low-thrust trajectory optimization approaches," *Aerospace*, vol. 8, no. 3, pp. 88–126, 2021.

[11] F. Topputo and C. Zhang, "Survey of direct transcription for low-thrust space trajectory optimization with applications," in *Abstract and Applied Analysis*. New York, NY, USA: Hindawi, 2014.

[12] F. Fahroo and I. Ross, "Trajectory optimization by indirect spectral collocation methods," in *Proc. Astrodyn. Spec. Conf.*, 2000, Art. no. 4028.

[13] D. A. Benson, G. T. Huntington, T. P. Thorvaldsen, and A. V. Rao, "Direct trajectory optimization and costate estimation via an orthogonal collocation method," *J. Guid., Control, Dyn.*, vol. 29, no. 6, pp. 1435–1440, 2006.

[14] P. J. Enright and B. A. Conway, "Optimal finite-thrust spacecraft trajectories using collocation and nonlinear programming," *J. Guid., Control, Dyn.*, vol. 14, no. 5, pp. 981–985, 1991.

[15] L. Hou-Yuan and Z. Chang-Yin, "Optimization of low-thrust trajectories using an indirect shooting method without guesses of initial costates," *Chin. Astron. Astrophys.*, vol. 36, no. 4, pp. 389–398, 2012.

[16] H. G. Bock and K.-J. Plitt, "A multiple shooting algorithm for direct solution of optimal control problems," *Int. Fed. Autom. Control Proc. Vols.*, vol. 17, no. 2, pp. 1603–1608, 1984.

[17] C. Zhang, F. Topputo, F. Bernelli-Zazzera, and Y.-S. Zhao, "Low-thrust minimum-fuel optimization in the circular restricted three-body problem," *J. Guid., Control, Dyn.*, vol. 38, no. 8, pp. 1501–1510, 2015.

[18] J. Senent, C. Ocampo, and A. Capella, "Low-thrust variable-specific-impulse transfers and guidance to unstable periodic orbits," *J. Guid., Control, Dyn.*, vol. 28, no. 2, pp. 280–290, 2005.

[19] D. Pérez-Palau and R. Epenoy, "Fuel optimization for low-thrust Earth–Moon transfer via indirect optimal control," *Celestial Mechanics Dynamical Astron.*, vol. 130, pp. 1–29, 2018.

[20] M. Rasotto, R. Armellin, P. Di Lizia, and F. Bernelli-Zazzera, "Optimal low-thrust transfers in two-body and three-body dynamics," in *Proc. 64th Int. Astronautical Congr.*, 2014, pp. 5230–5244.

[21] N. L. O. Parrish, "Low thrust trajectory optimization in cislunar and translunar space," Ph.D. dissertation, Univ. of Colorado, Boulder, CO, USA, 2018.

[22] J. F. Herman, "Improved collocation methods to optimize low-thrust, low-energy transfers in the earth-moon system," Ph.D. dissertation, Univ. of Colorado, Boulder, CO, USA, 2015.

[23] C. Martin and B. A. Conway, "Optimal low-thrust trajectories using stable manifolds," in *Spacecraft Trajectory Optimization*. Cambridge, U.K.: Cambridge Univ. Press, 2010, pp. 238–262.

[24] G. Mingotti, F. Topputo, and F. Bernelli-Zazzera, "Optimal low-thrust invariant manifold trajectories via attainable sets," *J. Guid., Control, Dyn.*, vol. 34, no. 6, pp. 1644–1656, 2011.

[25] Y. Kayama, K. C. Howell, M. Bando, and S. Hokamoto, "Low-thrust trajectory design with successive convex optimization for libration point orbits," *J. Guid., Control, Dyn.*, vol. 45, no. 4, pp. 623–637, 2022.

[26] A. Abraham, D. Spencer, and T. Hart, "Preliminary optimization of low-thrust, geocentric to halo orbit, transfers via particle swarm optimization," in *Proc. 24th AAS/Amer. Inst. Aeronaut. Astronaut. Space Flight Mechanics Meeting*, 2014, pp. 1–17.

[27] E. Taheri and O. Abdelkhalik, "Fast initial trajectory design for low-thrust restricted-three-body problems," *J. Guid., Control, Dyn.*, vol. 38, no. 11, pp. 2146–2160, 2015.

[28] A. D. Cox, K. C. Howell, and D. C. Folta, "Trajectory design leveraging low-thrust, multi-body equilibria and their manifolds," *J. Astronautical Sci.*, vol. 67, pp. 977–1001, 2020.

[29] D. H. Kuettel III and J. W. McMahon, "Low-thrust maneuverability using bilinear tangent guidance near small bodies," *J. Guid., Control, Dyn.*, vol. 44, no. 8, pp. 1425–1439, 2021.

[30] V. Troianskyi, V. Kashuba, and Y. Krugly, "Photometry of selected asteroids on the OMT-800 telescope," *Minor Planet Bull.*, vol. 46, pp. 109–110, 2019.

[31] E. G. Fahnestock and D. J. Scheeres, "Simulation and analysis of the dynamics of binary near-Earth Asteroid (66391) 1999 KW4," *Icarus*, vol. 194, no. 2, pp. 410–435, 2008.

[32] J. Bellerose and D. J. Scheeres, "Restricted full three-body problem: Application to binary system 1999 KW4," *J. Guid., Control, Dyn.*, vol. 31, no. 1, pp. 162–171, 2008.

[33] Y. Shi, Y. Wang, and S. Xu, "Equilibrium points and associated periodic orbits in the gravity of binary asteroid systems:(66391) 1999 KW4 as an example," *Celestial Mechanics Dynamical Astron.*, vol. 130, pp. 1–26, 2018.

[34] D. J. Scheeres, B. G. Williams, and J. K. Miller, "Evaluation of the dynamic environment of an asteroid: Applications to 433 Eros," *J. Guid., Control, Dyn.*, vol. 23, no. 3, pp. 466–475, 2000.

[35] D. J. Scheeres et al., "Dynamical configuration of binary near-Earth asteroid (66391) 1999 KW4," *Science*, vol. 314, no. 5803, pp. 1280–1283, 2006.

[36] D. J. Scheeres, *Orbital Motion Strongly Perturbed Environments: Applications to Asteroid, Comet and Planetary Satellite Orbiters*. Berlin, Germany: Springer-Verlag, 2016.

[37] R. A. Werner and D. J. Scheeres, "Exterior gravitation of a polyhedron derived and compared with harmonic and mascon gravitation representations of asteroid 4769 Castalia," *Celestial Mechanics Dynamical Astron.*, vol. 65, pp. 313–344, 1996.

[38] R. Brusch, "Bilinear tangent yaw guidance," in *Proc. Guid. Control Conf.*, 1979, Art. no. 1730.
[39] D. H. Kuettel III and J. W. McMahon, "Autonomous maneuver targeting around small bodies using continuous-thrust propulsion," *J. Guid., Control, Dyn.*, vol. 45, no. 3, pp. 499–516, 2022.
[40] N. Jorge and J. W. Stephen, *Numerical Optimization*. Berlin, Germany: Springer-Verlag, 2006.
[41] R. Zhang, Y. Wang, Y. Shi, and S. Xu, "Libration points and periodic orbit families near a binary asteroid system with different shapes of the secondary," *Acta Astronautica*, vol. 177, pp. 15–29, 2020.
[42] W. S. Koon, M. W. Lo, J. E. Marsden, and S. D. Ross, "Dynamical systems, the three-body problem," *Space Mission Des.*, 2006.
[43] M. J. Walker, B. Ireland, and J. Owens, "A set modified equinoctial orbit elements," *Celestial Mechanics*, vol. 36, no. 4, pp. 409–419, 1985.
[44] W. H. Press, *Numerical Recipes, 3rd Edition: The Art of Scientific Computing*. Cambridge, U.K.: Cambridge Univ. Press, 2007.
[45] Busek Space and Propulsion Systems, "BHT-600 Busek Hall effect thruster data sheet," Nov. 27, 2023. [Online]. Available: https://www.busek.com/bht600
[46] J. Polk et al., "Performance of the NSTAR ion propulsion system on the deep space one mission," in *Proc. 39th Aerosp. Sci. Meeting Exhibit.*, 2001, pp. 965–987.
[47] M. Patterson, J. Foster, T. Haag, V. Rawlin, G. Soulas, and R. Roman, "NEXT: NASA's evolutionary xenon thruster," in *Proc. 38th Amer. Inst. Aeronaut. Astronaut./Amer. Soc. Mech. Engineers/Soc. Automot. Engineers/Amer. Soc. Eng. Educ. Joint Propulsion Conf. Exhibit*, 2002, Art. no. 3832.
[48] Busek Space and Propulsion Systems, "BHT-8000 Busek Hall effect thruster data sheet," Accessed: Nov. 27, 2023. [Online]. Available: https://www.busek.com/index_htm_files/70000703%20BHT-8000%20Data%20Sheet%20Rev-.pdf
[49] D. L. Richardson, "Analytic construction of periodic orbits about the collinear points," *Celestial Mechanics*, vol. 22, no. 3, pp. 241–253, 1980.

Zicen Xiong received the B.Eng. degree in aerospace engineering, in 2022, from the School of Astronautics, Beihang University, Beijing, China, where he is currently working toward the master's degree in aerospace engineering.

His research interests include astrodynamics, circular restricted three-body problem, and nonlinear dynamics.

Yue Wang received the B.Eng. and Ph.D. degrees in aerospace engineering from Beihang University (formerly known as the Beijing University of Aeronautics and Astronautics), Beijing, China, in 2009 and 2014, respectively.

From 2014 to 2015, he worked as a Postdoctoral Fellow with the Distributed Space Systems Lab, Faculty of Aerospace Engineering, Technion—Israel Institute of Technology, Haifa, Israel. In 2016, he joined the School of Astronautics, Beihang University, as an Associate Professor. He was the author or coauthor of 100 publications in journals, books, and proceedings. His research interests include the astrodynamics, dynamics, and control about small celestial bodies.